JOURNAL OF GEOPHYSICAL RESEARCH, VOL. 104, NO. D22, PAGES 27,421–27,440, NOVEMBER 27, 1999

# A model for the natural and anthropogenic aerosols over the tropical Indian Ocean derived from Indian Ocean Experiment data

S.K. Satheesh,[1] V. Ramanathan,[1] Xu Li-Jones,[1] J.M. Lobert,[1] I. A. Podgorny,[1] J.M. Prospero,[2] B.N. Holben,[3] and N.G. Loeb[4]

**Abstract.** The physical, chemical and radiative properties of aerosols are investigated over the tropical Indian Ocean during the first field phase (FFP) of the international Indian Ocean Experiment. The FFP was conducted during February 20 to March 31, 1998. The results shown here are from the Kaashidhoo Climate Observatory (KCO), a new surface observatory established on the tiny island of Kaashidhoo (4.965°N, 73.466°E) in the Republic of Maldives. From simultaneous measurements of aerosol physical, chemical, and radiative properties and the vertical structure from lidar, we have developed an aerosol model which, in conjunction with a Monte Carlo radiative transfer model, successfully explains (within a few percent) the observed solar radiative fluxes at the surface and at the top of the atmosphere. This agreement demonstrates the fundamental importance of measuring aerosol physical and chemical properties for modeling radiative fluxes. KCO, during the northeast monsoon period considered here, is downwind of the Indian subcontinent and undergoes variations in the aerosol visible optical depth $\tau_v$ from ~0.1 to 0.4, with a monthly mean of ~0.2. Lidar data suggest that the aerosol is confined largely to the first 3 kms. Sulfate and ammonium contribute ~29% to $\tau_v$; sea-salt and nitrate contributes ~17%; mineral dust contributes ~15%; and the inferred soot, organics, and fly ash contribute 11%, 20%, and 8% respectively. We estimate that anthropogenic sources may contribute as much as 65% to the observed $\tau_v$. We consider both an externally and an internally mixed aerosol model with very little difference between the two in the computed radiative forcing. The observed scattering coefficients are in the upper range of those reported for other oceanic regions, the single-scattering albedos are as low as 0.9, and the Angstrom wavelength exponents of ~1.2 indicate the abundance of submicron aerosols. In summary, the data and the model confirm the large impact of anthropogenic sources. The surface global fluxes (for overhead Sun) decrease by as much as 50 to 80 W $m^{-2}$ owing to the presence of the aerosols, and the top of the atmosphere fluxes increase by as much as 15 W $m^{-2}$, thus indicating that anthropogenic aerosols are having a large impact on the tropical Indian Ocean.

## 1. Introduction

Uncertainty in modeling radiative forcing in general and aerosol radiative forcing in particular is one of the largest source of uncertainties in predicting climate change [e.g., see *Hansen et al.*, 1998]. In this text, we adopt a rather broad definition for the term "aerosol radiative forcing." The effect of aerosols, both natural and anthropogenic, on the radiative fluxes is referred to as radiative forcing. The effect of aerosols on top of the atmosphere (TOA) radiative fluxes is TOA radiative forcing, on surface fluxes it is surface radiative forcing, and on atmospheric radiative fluxes it is atmospheric radiative forcing. The aerosol radiative forcing arises from their interaction (both direct and indirect) with solar radiation [*Charlson et al.*, 1987]. The interaction of aerosols with radiation involves both scattering and absorption of radiation (direct effect), and the relative effect of each of these processes depends on the refractive index and the size distribution of aerosols. The refractive index is determined by the chemical composition, while the size distribution is governed by microphysical and dynamical processes. As a result, the data for the physical, chemical, and optical properties of aerosols are important for estimating the aerosol-cloud-climate interactions.

Aerosol particles originate from different sources: sea salt from oceans, mineral dust from arid and semiarid locations, sulfate and nitrate from both natural and anthropogenic sources; and organic and carbonaccous aerosols from biomass burning and industrial combustion [*Andreae,* 1995]. Estimation of the effects of aerosols on climate is complicated by the fact that aerosols and their chemical composition, abundance, and size distribution are highly variable, both spatially and temporally [*Pilinis et al.*, 1995]. Most of the

[1] Scripps Institution of Oceanography, University of California, San Diego, La Jolla.
[2] Rosenstiel School of Marine and Atmospheric Science, University of Miami, Miami, Florida.
[3] NASA Goddard Space Flight Center, Greenbelt, Maryland.
[4] NASA Langley Research Center, Hampton, Virginia.



Paper number 1999 JD900478.
0148-0227/99/1999 JD900478$09.00

investigations on direct aerosol forcing have focused on sulfate aerosols because of their importance as an anthropogenic aerosol component [*Charlson et al.*, 1987, 1991, 1992; *Hegg et al.*, 1993; *Kiehl and Breigleb*, 1993]. However, aerosol forcing from biomass burning has also received attention during the last decade [*Crutzen and Andreae*, 1990; *Kaufman et al.*, 1990; *Penner et al.*, 1992].

The accuracy of the computed aerosol forcing relies mainly on the choice of the aerosol model. In the present study (which is carried out over regions adjacent to the tropical Indian Ocean), an aerosol model has been developed based on observations and has been used for estimating the radiative fluxes using a Monte Carlo radiative transfer model [*Podgorny et al.*, 1998]. The fundamental objectives of the study are threefold: (1) to develop a tool for interpreting aerosol chemical, optical, and radiative forcing from observations; (2) to understand the relative importance of various types of aerosols to the column optical depths and radiative forcing, and (3) to understand how aerosols are modifying the solar energy reaching the surface as well as that reflected back to space.

The oceanic regions adjacent to the Asian subcontinent are influenced by two contrasting air masses (continental and marine) associated with the Indian monsoon system. Indian summer monsoon usually starts by the end of May and continues until November. During this period, winds are mainly southwesterly or westerly. The winter monsoon (also called the northeast monsoon) becomes established toward the end of November and continues until April. During this period the prevailing winds are mostly calm and northeasterly. The seasonal changes in the Intertropical Convergence Zone (ITCZ), where the two contrasting air masses meet and are carried deep into the upper troposphere by the resulting convergence (updrafts associated with the ITCZ), cause significant changes in the aerosol characteristics and their spatial and temporal distributions [*Krishnamurti et al.*, 1998]. The Indian Ocean Experiment (INDOEX) was formulated to study the transport of continental aerosols across the ocean to the remote Indian Ocean regions (see *Ramanathan et al.*[1995, 1996] for more details). Pre-INDOEX cruises have clearly established [*Jayaraman* et al., 1998; *Krishnamurti et al.*, 1998; *Satheesh et al.*, 1998] that sulfates and other continental aerosols are transported thousands of kilometers into the equatorial Indian Ocean (as far south as 5°S) with significant reduction in the solar radiation at the ocean surface. This study is a logical continuation of the earlier studies.

The results described in this paper are obtained from the data collected during the Indian Ocean Experiment first field phase (FFP), conducted during February 20 to March 30, 1998. The unique aspects of the present study are as follows: (1) It employs simultaneous data for the chemical, optical, and radiative effects of aerosols (2) The composite data are used to develop an aerosol model for the tropical Indian Ocean, influenced by continental pollution (3) The resulting aerosol optical model explicitly accounts for different species including sea salt, sulfates, nitrates, mineral dust, and soot (4) The radiative properties, i.e., scattering cross section, absorption cross section, and the phase function, are introduced in a Monte Carlo model separately for each species, thus avoiding the conventional practice of a priori averaging of optical properties.

## 2. Experimental Setup and Data

During 1998, the Center for Clouds, Chemistry and Climate ($C^4$) established the Kaashidhoo Climate Observatory (KCO) on the island of Kaashidhoo in the Republic of Maldives. Maldives consists of a group of small islands forming a long, narrow belt spread over the Arabian Sea extending along north-south from ~8°N to ~0°S. Kaashidhoo (4.965°N, 73.466°E) is a small, crescent-shaped island ~3 km long and slightly more than a km wide, isolated from the nearby islands (~20 km from the nearest Maldivian island) and is ~700 km away from the nearest main land, the Indian subcontinent. The population of the island is ~1600 and is free from anthropogenic activities such as industries or automobile transport. This tiny island can be considered as a platform on the Arabian Sea and the aerosol characteristics observed from this location, December to March, would represent those transported over the ocean from the nearby continents plus those produced naturally over the ocean surface. The island is characterized by its remote location away from major human activities. The observatory is located on the northeast tip of the island, so that the local pollution-like burning in the island is naturally restricted at the observatory since the synoptic-scale winds are mostly northeasterly, during the period of interest. The synoptic-scale winds experienced in KCO are the trade winds associated with the Indian monsoons.

**Table 1.** Various Experimental Setups Used at Kaashidhoo Climate Observatory During the Indian Ocean Experiment First Field Phase

| | Parameters Measured | Instruments Used |
|---|---|---|
| 1 | aerosol optical depth (340, 380 440, 500, 670, 870, 940, and 1020 nm) | CIMEL radiometer of AERONET |
| 2 | aerosol mass concentration of different aerosol species | three stage high volume impactor |
| 3 | direct solar flux (W $m^{-2}$), 0.28 to 2.8 μm | Kipp & Zonen normal incidence pyrheliometer |
| 4 | global and diffuse flux (W $m^{-2}$), 0.3 to 2.8 μm | Kipp & Zonen pyranometer, shaded and unshaded |
| 5 | aerosol scattering coefficient, 534 nm | integrating nephelometer, Radiance Research |
| 6 | aerosol absorption coefficient, 565 nm | particle soot/absorption photometer, Radiance Research |
| 7 | aerosol vertical structure | SABL lidar, pulsed, 0.532 and 1.064 μm, operated and developed by the NCAR |
| 8 | top-of-the-atmosphere flux | CERES satellite radiation budget data |

Abbreviations are defined as follows: CIMEL is the company name of the radiometer used; AERONET, Aerosol Robotic NETwork; SABL, Scanning aerosol backscatter lidar; CERES, Clouds and Earth's Radiant Energy System.

A list of instruments used in the present study is listed in Table 1. The CIMEL instrument at KCO is part of the AErosol RObotic NETwork (AERONET), which is a ground-based aerosol monitoring network and data archive supported by NASA's Earth Observing Systems (EOS). CIMEL is an autotracking solar radiometer that measures the field-limited solar radiation at eight narrow spectral bands from 340 to 1020 nm. The band at 940 nm is used for estimating the columnar water content and the other seven are used for the study of aerosols. The field of view (which determines the amount of diffuse radiation entering into the radiometer) of the CIMEL radiometer is 1.2°. This is small enough that the error caused by the diffuse light entering into the CIMEL's field of view should be <1% when the relative air mass (a geometrical term to account for the relative increase in the optical path length as solar zenith angle increases) is <2.0 [see *Box* and *Deepak*, 1979]. The resulting uncertainty in the CIMEL-measured aerosol optical depth is <±0.01 [*Holben et al.*, 1998]. More details about the CIMEL radiometer are described by *Holben et al.* [1998].

The total aerosol concentrations in three size ranges were measured daily by drawing ambient air through a three-stage impactor at a flow rate of ~47 $m^3$ $h^{-1}$ for ~24 hours. Slotted Whatman 41 (W-41) filters were used as the impaction surface. In order to avoid contamination from local sources, wind sensors were used to control the pumps, which were activated only when winds blew from the ocean at a speed >1 m $s^{-1}$. In the marine boundary layer the collection efficiency of W-41 filters is >99% for non-sea-salt (nss) $SO_4^=$ [*Pszenny et al.*, 1993]; 95% for $NO_3^-$, and 99% for dust [*Savoie and Prospero*, 1982]. The filters were changed every evening. The exposed bulk filters were sealed separately in plastic bags in a particle-free clean hood at the site and sent to University of Miami for chemical analysis. In Miami, a quarter of each bulk filter and half of each impactor substrate were extracted with 20 mL of 18 $M\Omega$cm milli-Q water in three separate aliquots of 10, 5, and 5 mL. Sample solutions were measured for $Na^+$ with a standard deviation of ±2% by flame atomic absorption, for $NO_3^-$, $SO_4^=$ within ±5% by suppressed ion chromatography and for $NH_4^+$ within ±10% by automated calorimeter [*Savoie et al.*, 1989]. The nss $SO_4^=$ is calculated as the total $SO_4^=$ minus $Na^+$ concentration times 0.2517 (i.e., $SO_4^=$:$Na^+$ mass ratio in bulk seawater). The total sea salt is estimated by multiplying the $Na^+$ by 3.25. The mineral dust is determined by ashing the extracted filters at 500°C for ~14 hours and weighing the residue (ash). The standard error in the mineral aerosol concentration is ±10% for concentrations >~1 μg $m^{-3}$; below 1 μg $m^{-3}$ the standard error is essentially constant at ±0.1 μg $m^{-3}$. Please note that during the extraction process, some components are dissolved, and during heating process volatile materials (e.g., organic materials) may be lost.

The pyranometers (ventilated) and pyrheliometer used in the present study to measure the ground reaching solar (global, direct and diffuse) fluxes are from the Kipp & Zonen group. The instrument is designed for measuring the irradiance (W $m^{-2}$) on a plane surface. Since this instrument does not exhibit tilt dependence, it can measure solar radiation at high solar zenith angles as well. For measuring the diffuse component only, the direct component is shielded automatically by using a Sun tracker and shadow ball arrangement. The pyranometers that were purchased just before the start of this study are calibrated at Kipp & Zonen as well as at National Oceanographic and Atmospheric Administration Climate Monitoring and Diagnostic Laboratory (NOAA CMDL), and the calibration coefficients (or responsivities, which is the ratio of the voltage output to the incident irradiance) provided by both of them agree within ±1%. The instrument is characterized by its high sensitivity, low impedance, low temperature response, and low nonlinearity. While at field, the instrument was cleaned every morning before sunrise.

The Radiance Research (model M903) portable nephelometer is designed to measure the light-scattering coefficient using the geometry of a standard integrating nephelometer. Pressure and temperature sensors automatically correct for changes in Rayleigh scattering. The light source is a variable-rate flash lamp with a filter, which has a narrow passband at 530 nm. The optical and electrical background noise is sufficiently low to allow measurement of the aerosol scattering coefficient from >10% of Rayleigh ($1.3 \times 10^{-6}$ $m^{-1}$) to greater than 1 $km^{-1}$.

The particle soot/absorption photometer (PSAP) is used to measure the near-real-time aerosol absorption coefficient. The instrument works on the basic principle of Beer's law, in which the change in optical transmission of a filter caused by particle deposition is related to the optical absorption coefficient and a calibration transfer coefficient. The instrument can be operated continuously to obtain a time series of the aerosol absorption coefficient.

The scanning aerosol backscatter lidar (SABL) operates at two wavelengths, 0.532 (green) and 1.032 μm (near infrared (IR)). It has a power of 120 mJ (which is split 1/3 green and 2/3 IR) and an adjustable beam width of 1 to 4 mrad. It can pulse at up to 60 pulse $s^{-1}$. The pulses are 15 ns long (2.25 m). The field of view of the telescope is also adjustable between 1 and 4 mrad. Typically, the profiles are averaged at 1-s timescales before the data are analyzed.

## 3. Observed Aerosol Characteristics and Aerosol Model

The development of the model from the various data consist of the following iterative steps: (1) The starting point is the standard oceanic model of *Hess et al.* [1998] for the size distribution of sea salt, sulfates, nitrates, ammonium, and mineral dust. (2) The number of aerosol species in each size range is adjusted until the mass of each species agrees with the measured mass at KCO in the three size ranges. (3) To this size distribution, size-dependent soot aerosols are added until the surface single-scattering albedo agrees with the measured values. (4) The aerosol is assumed to be externally mixed. (5) LIDAR back scattered data are used to approximate the vertical profile of aerosol. (5) The columnar wavelength-dependent aerosol optical depth is computed next and compared with the measured optical depths. The difference between the two (the measured was always larger) is attributed to aerosols that have not been measured (e.g., organics and dust layers aloft). The size distribution of the "missing" aerosols is inferred by adjusting the calculated aerosol optical depths to agree with the observed spectral variation of the optical depths.

However, we also consider an internally mixed aerosol model and show that the two aerosol models have very similar radiative effects. The model is validated by comparing the aerosol radiative forcing computed by the model with the observed fluxes.

### 3.1. Observed Aerosol Characteristics

Since the properties of aerosols (both transported from the continents and produced naturally) depend on the prevailing meteorological conditions, a description of the general meteorological features observed at KCO (during the FFP) is given first. The daily mean wind speed and wind direction observed at the observatory is shown in Figure 1. The surface winds during FFP were mainly northeasterly or northerly. The wind speeds were generally low in the range 2 to 4 m $s^{-1}$, but occasionally exceeded 7 m $s^{-1}$. However, we did not observe wind speeds >10 m $s^{-1}$ during this period. Being a tiny island over the vast ocean, Kaashidhoo does not experience large diurnal variations in temperature or relative humidity. The daily mean values of relative humidity are shown in Figure 2 and varied from ~66% to ~77% during the FFP. Also shown (dotted line) in Figure 2 is the columnar precipitable water content (w in centimeters) retrieved from the CIMEL optical depth measurements (using 940 nm which is almost in the center of the ρστ water vapor absorption band and adjacent wavelengths (870 and 1020 nm) which are not influenced by the water vapor). Both relative humidity (RH) (percent) and w (centimeters) follow the same pattern, and any deviation in the pattern is attributed to the changes in the water vapor vertical profiles. Except for occasional drizzle of few millimeters, there was no rainfall during the FFP.

**3.1.1. Aerosol optical depths.** Since the CIMEL optical depths are available at several wavelengths, the measurements contains information about the aerosol size distribution. The aerosol optical depth data for clear skies are selected by using the solar flux (W $m^{-2}$) data from the pyranometers and the pyrheliometer. Several criteria are imposed to screen out the data influenced by clouds. The hourly running mean of flux at each measurement is compared with the adjacent measurements. If the running mean is less than an arbitrarily assigned percentage of the adjacent values, then the data points are rejected. Also, the data points are rejected by calculating the slope using adjacent data points and the unreasonable value of the slope results in the rejection of the point. If >50% of data points are rejected in any hour that hour bin is rejected as cloudy data.

A simple way of representing the spectral variation of aerosol optical depth is by using the Angstrom power law given by,

$$\tau_p = \beta \lambda^{-\alpha} \quad (1)$$

where $\alpha$ is the wavelength exponent, $\beta$ is the turbidity parameter, and $\lambda$ is the wavelength in μm. (In this paper, the symbol $\tau_p$ is used for aerosol spectral optical depth and $\tau_v$ is for aerosol optical depth at 500 nm). The value of $\alpha$ depends on the ratio of the concentration of large to small aerosols, and $\beta$ represents the total aerosol loading in the atmosphere [*Shaw et al.*, 1973]. The values of $\alpha$ and $\beta$ are obtained by least squares fitting of the spectral optical depths in a log-log scale. The temporal variation of the aerosol optical depth at three representative CIMEL wavelengths (lying in the UV, visible, and NIR regions) are shown in Figure 3a. Figure 3b shows the temporal variations of daily mean $\tau_p$ at 500 nm and the Angstrom wavelength exponent. The vertical bars represent standard deviations. Scattering of radiation by aerosols in the visible to near-IR wavelengths is strongly dependent on the aerosol size. In general, the scattering cross section decreases with increasing wavelength for fine

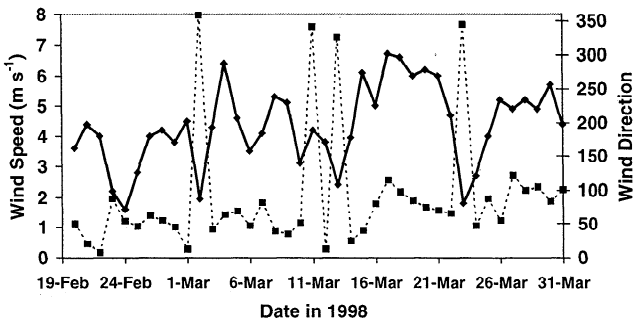


Figure 1. Daily average wind speed (solid line) and wind direction (dotted line).

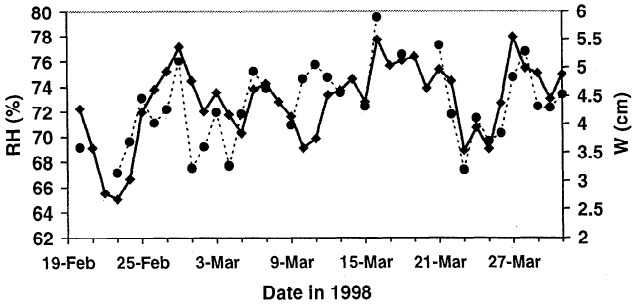


Figure 2. Temporal variations of relative humidity (solid line) and columnar perceptible water content (dotted line).

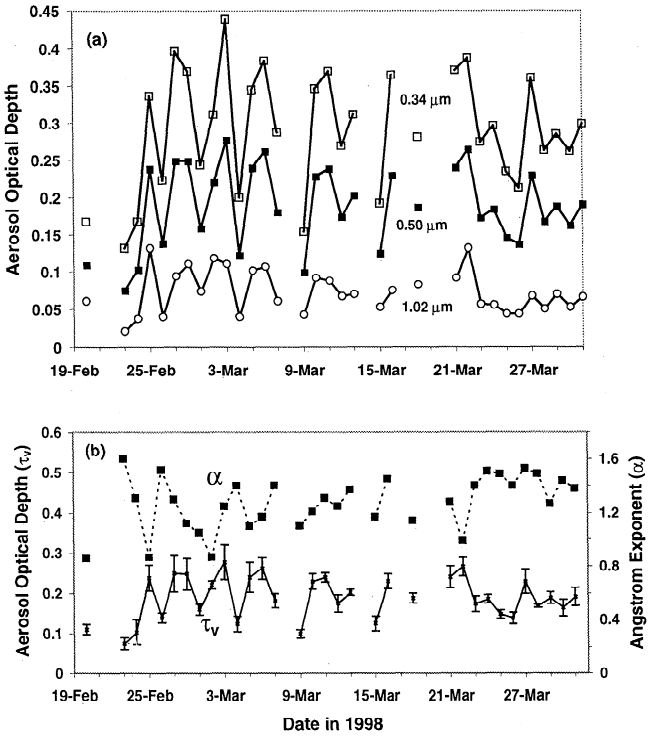


Figure 3(a). Temporal variation of daily mean aerosol optical depth at three representative CIMEL wavelengths. (b) Temporal variation of daily mean aerosol optical depth at 500 nm (solid line), with vertical bars representing standard deviations. Also shown is the variation of daily mean Angstrom wavelength exponent (dotted line).

aerosols. As the size increases, however, the wavelength dependence decreases such that when the aerosol radius exceeds a few microns, the scattering cross section is almost independent of wavelength. As a result, the temporal and spatial variations in the spectral dependence of optical depths are indicative of variations in size distribution.

It can be seen from the Figure 3 that $\tau_p$ at NIR wavelengths follows the same pattern as that of the visible wavelengths and the value of $\alpha$ is more or less steady. This suggests that the aerosol size distribution remains more or less the same (at least the basic shape) during the FFP. This inference is also supported by the fact that there were not many drastic changes (see Figure 2) in the wind direction, with the exception of a few events associated with the local (low) pressure systems. The high values of the $\alpha$ (>1.0 most of the time) at this island location far away from the continents is surprising, since the spectral variations of aerosol optical depth over the oceanic regions are expected to be less and hence a lower value of $\alpha$ (<0.6) [*Satheesh and Moorthy*, 1997]. In this case the value of $\alpha$ never falls below 0.6 but remains at around 1.2. Because of the inhomogenity and the aerosol source contrast over the land areas surrounding the KCO, it is reasonable to expect that different air masses carry different types of aerosols, depending on their origin. The back trajectories of wind pattern have been used to approximate the origin of the air masses that have encountered at Kaashidhoo. It has been observed that the surface flow is northeasterly most of the time.

Some typical examples of the spectral variations of aerosol optical depth, are shown in the Figure 4. During March 7, surface observations (mass concentrations of different chemical species) show that the sulfate component is dominating, and examination of back trajectories of air masses (T.N. Krishnamurti, private communication, 1998) have shown that the winds are from the Indian subcontinent. During March 1, the dust content is found to dominate and the back trajectories reveal an air mass from east of Kaashidhoo. Since the dust component used here contains all refractory materials (as is evident from the extraction process described in section 2), the primary products (those which are not completely burned) of burning (e.g., biomass) from locations north and east of Kaashidhoo, which are expected to be larger in size, could be the reason for the enhancement in the near-infrared wavelengths. At the same time the polluted air (which contains fine aerosols) from the Indian subcontinent are not influencing the aerosol features at KCO in this case, which explains the decrease in the visible aerosol optical depths. February 23 represents a day when all the components showed low values (clean day) and is one of the extreme cases of low $\tau_p$, with most days following the pattern similar to that of March 7. The sharp decrease in aerosol optical depth with wavelength (which is also evident from Figure 3) strongly suggests the presence of small aerosols over the observation location (KCO). A significant portion of the small aerosols could be the result of transport from the Indian subcontinent. The mean values and standard deviations of aerosol optical depths are shown in Table 2 and those of $\alpha$ and $\beta$ are given in Table 3.

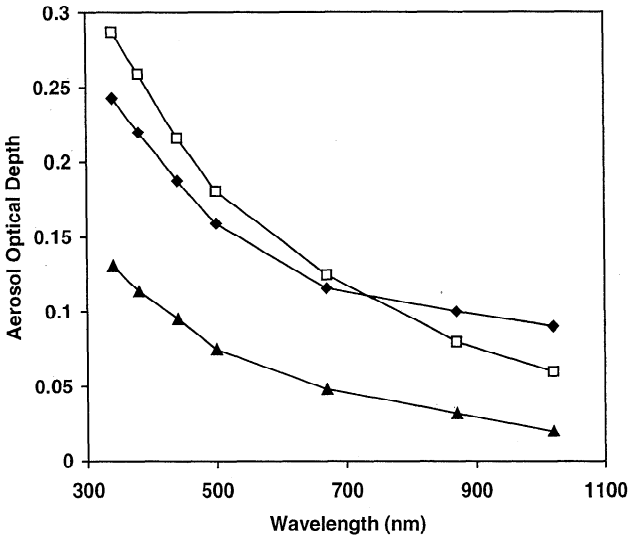


Figure 4. Spectral variation of aerosol optical depth (daily mean) on three representative days, March 1 (diamonds), March 7 (squares), and February 23 (triangles), which are influenced by different air mass, types.

**Table 2.** Mean Values of Aerosol Optical Depths during INDOEX FFP 1998

| Wavelength λ, nm | Aerosol Optical Depth $\tau_p(\lambda)$ | Standard Deviation |
|---|---|---|
| 340 | 0.289 | 0.079 |
| 380 | 0.262 | 0.073 |
| 440 | 0.221 | 0.062 |
| 500 | 0.188 | 0.055 |
| 670 | 0.125 | 0.038 |
| 870 | 0.098 | 0.030 |
| 1020 | 0.073 | 0.028 |

The higher values of $\tau_p$ on around of March 21 are found associated with a high-wind (though not so high) episode as can be seen from the Figure 1. Many investigators have found an enhancement in aerosol optical depth as wind speed increases [*Hoppel et al.*, 1990; *Satheesh et al.*, 1998]. The aerosol optical depths observed at KCO are analyzed to estimate their dependence on wind speed. An exponential type of increase in $\tau_p$ is observed with wind speed ($U$) of the form,

$$\tau_p(\lambda) = \tau_{p0}(\lambda)\exp[c(\lambda)U] \quad (2)$$

where $\tau_{p0}$ is the wind-independent component of aerosol optical depth and $c$ is the wind index, which represents the extent of wind dependence. The smaller the value of $c$, the smaller is the wind dependence. The values of the coefficients ($\tau_{p0}$ and $c$) and the corresponding correlation coefficients $\rho$ are given in Table 4. Since the aerosols over

**Table 3.** Mean Values of $\alpha$ and $\beta$ Observed During INDOEX FFP 1998

| | Wavelength Exponent $\alpha$ | Turbidity Parameter $\beta$ |
|---|---|---|
| Mean | 1.233 | 0.095 |
| Standard Deviation | 0.209 | 0.032 |

**Table 4.** Regression Coefficients of ln $\tau_p$ versus $U$

| Wavelength λ, nm | $\tau_{p0}$ | Wind Index $c$, s m$^{-1}$ | Correlation Coefficient ρ |
|---|---|---|---|
| 340 | 0.202 | 0.049 | 0.594 |
| 380 | 0.182 | 0.049 | 0.601 |
| 440 | 0.155 | 0.048 | 0.591 |
| 500 | 0.127 | 0.049 | 0.586 |
| 670 | 0.080 | 0.050 | 0.543 |
| 870 | 0.045 | 0.051 | 0.485 |
| 1020 | 0.030 | 0.051 | 0.482 |

marine environment are expected to be hygroscopic in nature, the observations (of $\tau_p$) at RH higher than 74% is not included in the above analysis, which avoids the influence from aerosol growth with RH. When RH is below 74% (deliquescence level), the aerosol growth is not expected to be significant [*Hanel*, 1976; *Cantrell et al.*, 1997].

The wind index $c$ observed in the present study is too low when compared with other investigations into the dependence of wind speed on aerosol characteristics. The different estimates of the wind index range from 0.27 [*Kulkarni et al.*, 1982] to 0.13 [*Prodi et al.*, 1983]. However, almost all of the previous measurements were carried out over remote oceanic regions where aerosol production by sea surface wind is a major contributor to the total aerosol loading. In the present case, however, the aerosol optical depths are, in general, high (Figure 3). Because of the proximity of the Indian subcontinent, the aerosol production by sea surface winds is only one of many causal factors for the total aerosol loading, the major contributor being the transport of fine anthropogenic aerosols from continental India. Furthermore, wind speed ranges observed during FFP were also low (1 to 8 m s$^{-1}$).

An examination of the temporal variations in RH (or $w$) [Figure 2] with that of $\tau_p$ (Figure 3) reveals that aerosol optical depth is correlated with RH. An enhancement in aerosol optical depth (500 nm) of ~0.0083 (RH index) per unit increase in RH was observed with a correlation coefficient of +0.53. To avoid the effect of aerosol production on wind speed, observations (of $\tau_p$) at wind speeds >4 m s$^{-1}$ (when $U$<4 m s$^{-1}$, hc aerosol production is expected to be zero [*Blanchard and Woodcock*, 1980] ) were not used in the correlation of $\tau_p$ versus RH. As a result, the coefficients (derived here) that define the enhancement of $\tau_p$ with RH and wind speed are considered independent of each other.

**3.1.2. Aerosol size distribution.** Since the spectral characteristics of the aerosol optical depths depend strongly on the aerosol size distribution, it is possible to infer the size distribution of aerosols from the spectral optical depth measurements and use this to validate the size distribution in the model. Out of several methods available for inverting size distributions, the constrained linear inversion technique by *King* [1982] has been used in the present study. This technique involves the numerical inversion of the integral equation given by

$$\tau_p(\lambda) = \int_{ra}^{rb} \pi r^2 Q_{ext}(m, r, \lambda) n_c(r) dr \qquad (3)$$

where $Q_{ext}$ is the aerosol extinction efficiency, factor which depends on the aerosol refractive index ($m$), radius ($r$), and wavelength of incident radiation λ; $n_c$ ($r$) is the columnar size distribution function of aerosols (number of aerosols in a vertical column of unit cross section in a small radius range $dr$ centered at $r$) and $r_a$ and $r_b$ are the lower and upper radii limits, respectively, of integration. The aerosols are assumed spherical. The technique involves discretizing the integral in (3) via quadrature formulas and solving the resulting matrix equation for $n_c(r)$ following the iterative inversion procedure described by *King* [1982] and as applied by *Satheesh et al.* [1998]. The solutions are constrained through the application of a smoothing matrix **H** which can be calculated from a finite difference formula [*Twomey*, 1977]. The resulting solution is expressed by,

$$\mathbf{n} = [\mathbf{A}^T\mathbf{C}^{-1}\mathbf{A} + \gamma\mathbf{H}]^{-1}\mathbf{A}^T\mathbf{C}^{-1}\tau_p \qquad (4)$$

where $\mathbf{n}$ is the vector containing the number density $n_i$ of size distribution function at radius $r_i$, A is the matrix of quadrature coefficients, and $\tau_p$ is the vector of aerosol spectral optical depths [$\tau_p(\lambda)$]. The parameter γ is a nonnegative Lagrange multiplier. The Lagrange multiplier is introduced following *King et al.* [1978] to achieve a fair degree of smoothing. Higher values of γ would mean higher smoothing because of the term γ**H** in (4). Choosing a too large value of γ overconstrains the solution and a too small value of γ can introduce false oscillations into the solution. Furthermore, *King* [1982] suggested that the value of the relative Lagrange multiplier (defined as $\gamma_{rel} = \gamma\mathbf{H}_{11} / [\mathbf{A}^T\mathbf{C}^{-1}\mathbf{A}]_{11}$ ) is important rather than γ by itself. As the value of $\gamma_{rel}$ is varied, solution vector elements approach asymptotic limits. The value of $\gamma_{rel}$ is varied in an iterative manner starting from a very low positive value in steps until all the solution vectors become positive and the retrieved size distributions yield aerosol optical depths that agree with the measured $\tau_p$ (λ) within the expected measurement errors. The values of $r_a$ and $r_b$ have been taken as 0.05 and 3.0 μm, respectively, as they are found to be optimal by examining the kernel functions (integrand of (3)), corresponding to the extreme wavelengths used here.

The complex refractive index values are assumed wavelength dependent, and the values given by *d'Almeida et al.* [1991] and *Hess et al.* [1998] have been used consistent with the aerosol model to be described in the following sections. Additional relevant details are given by *Jorge and Ogren* [1996] and *Satheesh et al.* [1998]. The size distributions retrieved in this manner reveal bimodal characteristics. The physical parameters of the retrieved size distribution such as the mode radii $r_{mi}$ and standard deviation $\sigma_{mi}$ are determined by least square fitting a bimodal lognormal distribution function of the form

$$n(r) = \sum_{i=1}^{2} \frac{N_{0i}}{\sqrt{2\pi}\log\sigma_{mi} r \ln(10)} \exp\left[-\frac{1}{2}\left(\frac{\log r - \log r_{mi}}{\log\sigma_{mi}}\right)^2\right] \qquad (5)$$

where $r_{mi}$ and $\sigma_{mi}$ are the mode radii and standard deviations, respectively. The $i$=1 represents the primary (small aerosol) mode and $i$=2 represents the secondary (large aerosol) mode and the parameter $N_0$ depends on the total aerosol concentration.

The effective radius $r_{eff}$ (which is a measure of the total volume to the surface area of a distribution of aerosol particles) and columnar mass loading ($m_L$) are determined using the following equations:

$$r_{eff} = \frac{\int_{r_a}^{r_b} r^3 n_c(r)dr}{\int_{r_a}^{r_b} r^2 n_c(r)dr} \quad (6)$$

$$m_L = \frac{4}{3}\pi r^3 d n_c(r)dr \quad (7)$$

where $d$ is the density of aerosols assumed to be 1.8 g cm$^{-3}$ and $n_c$ $(r)$ is the columnar size distribution function of aerosols defined by (5).

The significance of $r_{eff}$ and $m_L$ is that the variations in $m_L$ show the variations in the total aerosol loading, irrespective of the size distributions (since an increase in both small and large aerosols can increase the aerosol mass load), whereas the variations in $r_{eff}$ tell us whether the increase in $m_L$ is caused by small aerosols or large aerosols (since the relative increase in the larger aerosols increases the value of $r_{eff}$ and a relative increase in the smaller aerosols decreases the value of $r_{eff}$) [*Moorthy et al.*, 1998]. The mean values of $r_{eff}$ and $m_L$ observed during FFP are 0.331±0.077 μm and 103.23±33.71 mg m$^{-2}$, respectively. Both $r_{m1}$ and $r_{m2}$ (mode radii) do not show any significant variations during FFP except random fluctuations. The mean values of the mode radii $r_{mi}$ and standard deviations $\sigma_{mi}$ estimated during the FFP are shown in Table 5.

The bimodal size distribution is typical of observations in marine environments. The size distribution is mainly determined by the relative strength of different production and removal processes [*Jaenicke*, 1993]. After production, the small particle end of the size distribution is controlled mainly by coagulation and large particle end is controlled by sedimentation [*Pruppacher and Klett*, 1978]. Besides, the various microphysical processes bring about continuous size transformations and are quite important in limiting the concentrations of extremely small particles (r<0.01 μm). The size distribution of aerosols over marine locations depends on a number of additional processes including the long-range transport of aerosols from the nearby continents [*Prospero*, 1979; *Tyson et al.*, 1996], local production at the sea surface [*O'Dowd and Smith*, 1993], and processes such as nonprecipitating cloud cycling [*Hoppel et al.*, 1994]. The inversion of sky radiance measurements using a similar CIMEL radiometer in the mid-Atlantic region of the eastern United States that was influenced by urban/industrial pollution has shown an accumulation mode (for high optical depths) at 0.11 μm and a sea-salt mode at 0.99 μm, which are comparable with the values of $r_{m1}$ and $r_{m2}$ in the present study [*Remer and Kaufman*, 1998].

**Table 5.** Mean Values of $r_{mi}$ and $\sigma_{mi}$

| | Mode Radii $r_{m1}$, μm | log $\sigma_1$ | Mode Radii, $r_{m2}$, μm | log $\sigma_2$ |
|---|---|---|---|---|
| Mean | 0.135 | 0.394 | 0.955 | 0.312 |
| Standard Deviation | 0.032 | 0.042 | 0.142 | 0.051 |

Here subscripts 1 and 2 refer to modes 1 and 2, respectively; log σ denotes standard deviation.

The simultaneous measurements of aerosol size distribution (in the range 0.005 < r <20 μm) and cloud droplet spectra made in a cloud-topped marine boundary layer within 50 km of the Oregon coast by *Hoppel et al.* [1994] have also shown two distinct modes in the aerosol size distribution (in the range 0.1 to 10 μm), the small aerosol mode at ~0.2 μm and the large aerosol mode at ~2 to 3 μm. From a comparison of size distribution of interstitial aerosol within the cloud with that below the cloud, they concluded that the mode at ~0.2 μm is the result of processing of aerosols through (nonprecipitating) cloud cycles. The large aerosol mode observed in the present study may be composed of sea-salt aerosol produced from the ocean surface and the mineral dust transported from the nearest continents.

**3.1.3. Vertical profiles.** Earlier studies on the vertical distribution of aerosols over the oceans have revealed that the marine boundary layer consists of mainly two layers, the upper cloud layer and the lower subcloud layer [*Blanchard and Woodcock*, 1980]. The subcloud layer, ~500-1000 m thick, is generally well mixed and characterized by an adiabatic lapse rate. The lapse rate tends to become stable within the cloud layer. In correspondence with the above two layers, vertical structure of aerosols over the oceans also reveals two layers. In the upper layer aerosol, concentration drops with an increase in altitude in an almost exponential manner, while the size distribution is roughly the same with height especially in the marine boundary layer. *Kristament et al.* [1993] have estimated a value of 900 m for the scale height of vertical distribution of sea-salt aerosols over the southwest Pacific regions.

The SABL Lidar in the tropical Indian Ocean (in the vicinity of KCO) reveal a similar double layer: a dense aerosol layer of ~1 km thick adjacent to the ocean and an overlying layer where the aerosol seems to decrease with altitude (Plate 1). Consistent with prior oceanic data and the back-scattered profile from SABL Lidar, we assume the following vertical profile: a 1 km-thick mixed layer immediately above the ocean where the aerosol concentration is assumed to be constant with altitude, and, above this, the aerosol concentration is assumed to decrease exponentially with a scale height of 800 m.

**3.1.4. Aerosol chemical composition.** To evaluate the optical properties of aerosols, it is necessary to identify the chemical species, that contribute to the total aerosol mass and to characterize typical size distributions for each of these components. The principal chemical species of aerosol are identified as sulfates, nitrates, silicates, sea salt, soot, and organic matter [e.g., *Hess et al.*, 1998]. In the present study, the aerosols are broadly classified into the following species: (1) sea salt; (2) non-sea-salt sulfates and ammonium (as a single component); (3) mineral dust (transported); (4) soot; (5) "ash," which could be originated as a result of biomass burning; and (6) all others, which includes organics (not measured at KCO) and aerosols aloft (e.g., layers), which are not accounted for in the assumed vertical profile. This classification follows *Hess et al.* [1998] and is constrained by the availability of the chemical data at KCO. In this classification the insoluble portion of aerosols is included in mineral dust. The Sea-salt component comprises two individual size distributions, accumulation (small aerosols) and coarse (large aerosols) modes. In the marine environment, nitrate was found apparently associated with sea-salt aerosol [*Savoie and Prospero*, 1982]. The mass size

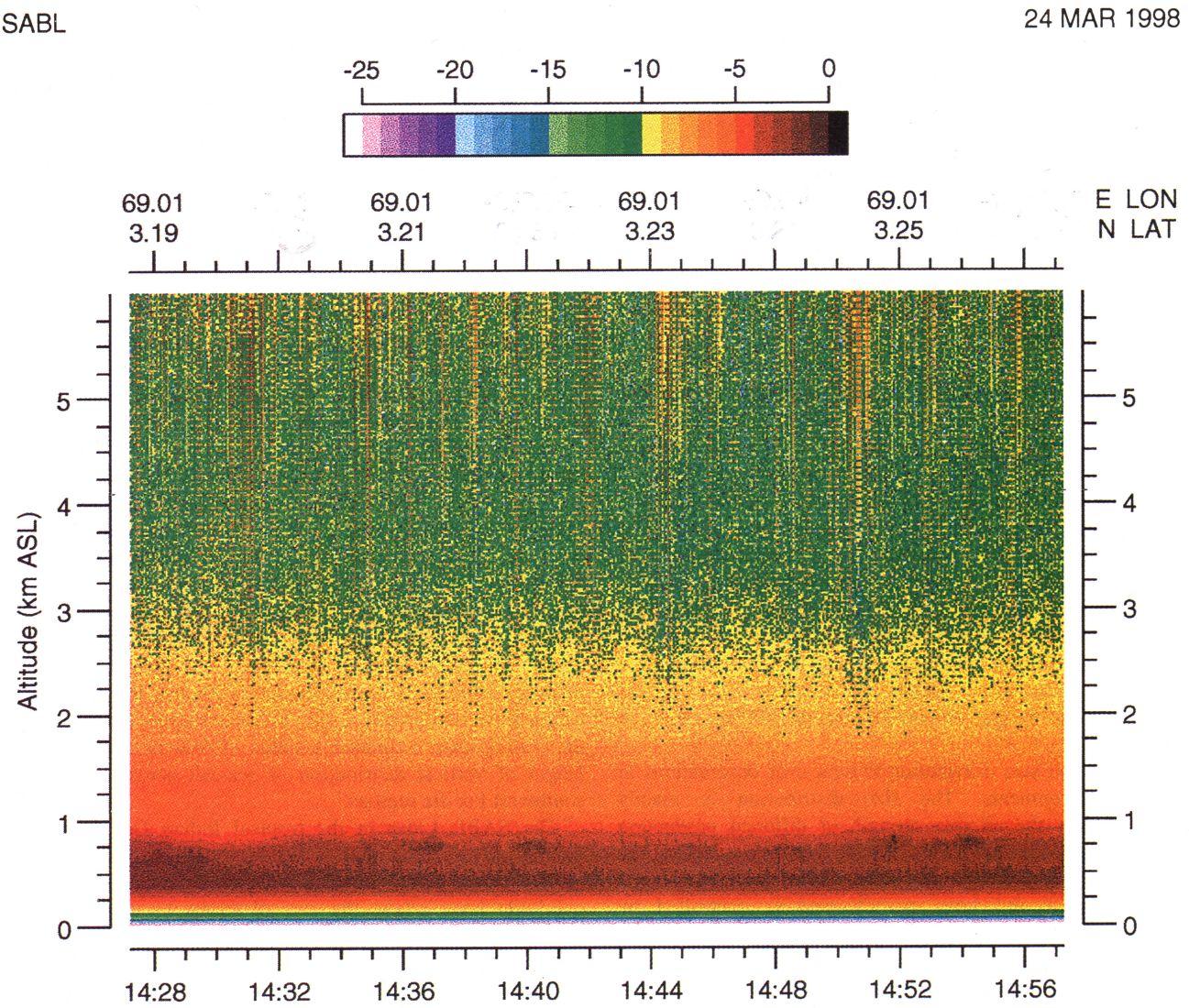


Plate 1. Relative backscatter (532 nm) from the scanning aerosol backscatter lidar as a function of altitude. The x axis represents universal time.

distribution of nitrate measured at KCO during FFP also shows a dominant coarse fraction. So we grouped the nitrate with sea-salt aerosol rather than with sulfate and ammonium as in Hess' model. Non-sea-salt sulfate and ammonium together form a single component, which represent the aerosols originating from gas-to-particle conversion (GPC) processes. This component is used to describe the anthropogenic aerosols. Mineral dust is those aerosols transported from the arid and semiarid locations adjacent to the observation site. The soot component is used to represent absorbing black carbon. Sulfate and soot present the in marine environment are often transported from polluted continental areas adjacent to the region of observation. Dimethylsulfide (DMS) produced by marine phytoplankton is another source of sulfur present in marine locations [*Charlson et al.*, 1987]. However, the organic aerosols (which are usually secondary products, i.e., formed in the atmosphere by the gas-to-particle conversion of volatile gaseous species) are smaller in size and can be transported long distances from the source regions [*Jaenicke,* 1993].

The mass concentrations (dry) of the chemical species measured at KCO are classified as described above, and the average mass concentrations during FFP at three size ranges are shown in Plate 2 as a percentage contribution of each chemical component.

### 3.2. Aerosol Model

**3.2.1. Chemical composition and size distribution.** The species considered here include sea salt, nitrate, non-sea-salt sulfate, mineral dust, and ammonium. Unless otherwise mentioned, the species are assumed to be externally mixed. The mass concentrations are averaged over the FFP period to get an estimate of the relative contribution in total aerosol mass of each chemical species. The aerosol size distributions for each of these species are generated by using standard values for the mode radius and standard deviation following *Hess et al.* [1998]. We used standard values for mode radii and standard deviation because of the absence of size distribution measurements of individual chemical species during FFP. The size distributions of each species are

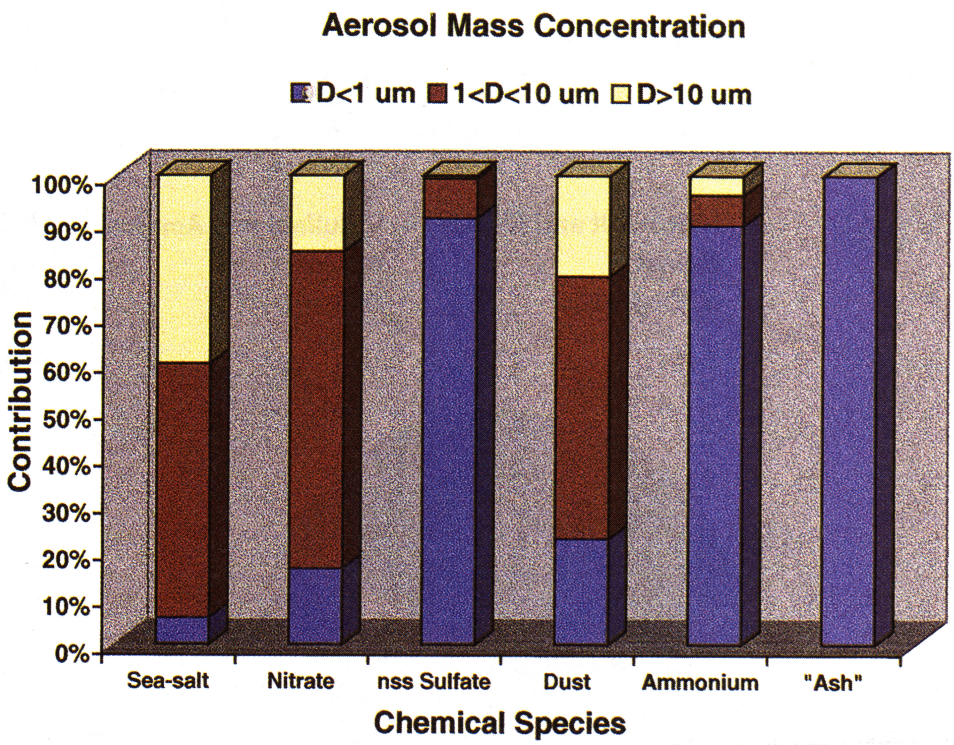


Plate 2. Distribution of aerosol mass concentration (percent contribution) of various chemical species as a function of size (mean values during the first field phase).

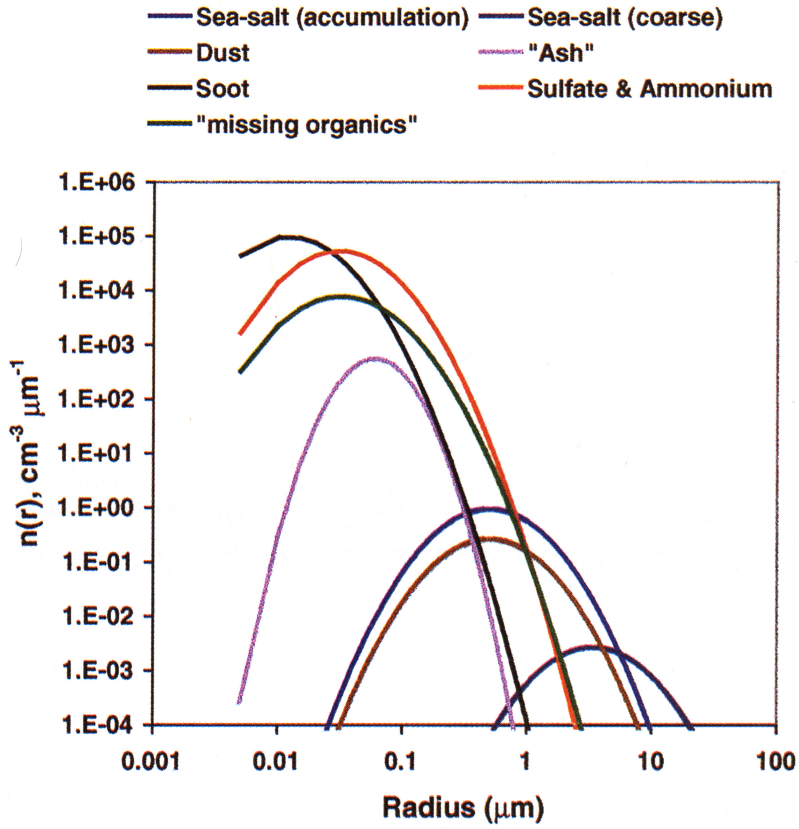


Plate 3. Size distribution of different chemical species obtained from the mass distribution (FFP mean) of individual species.

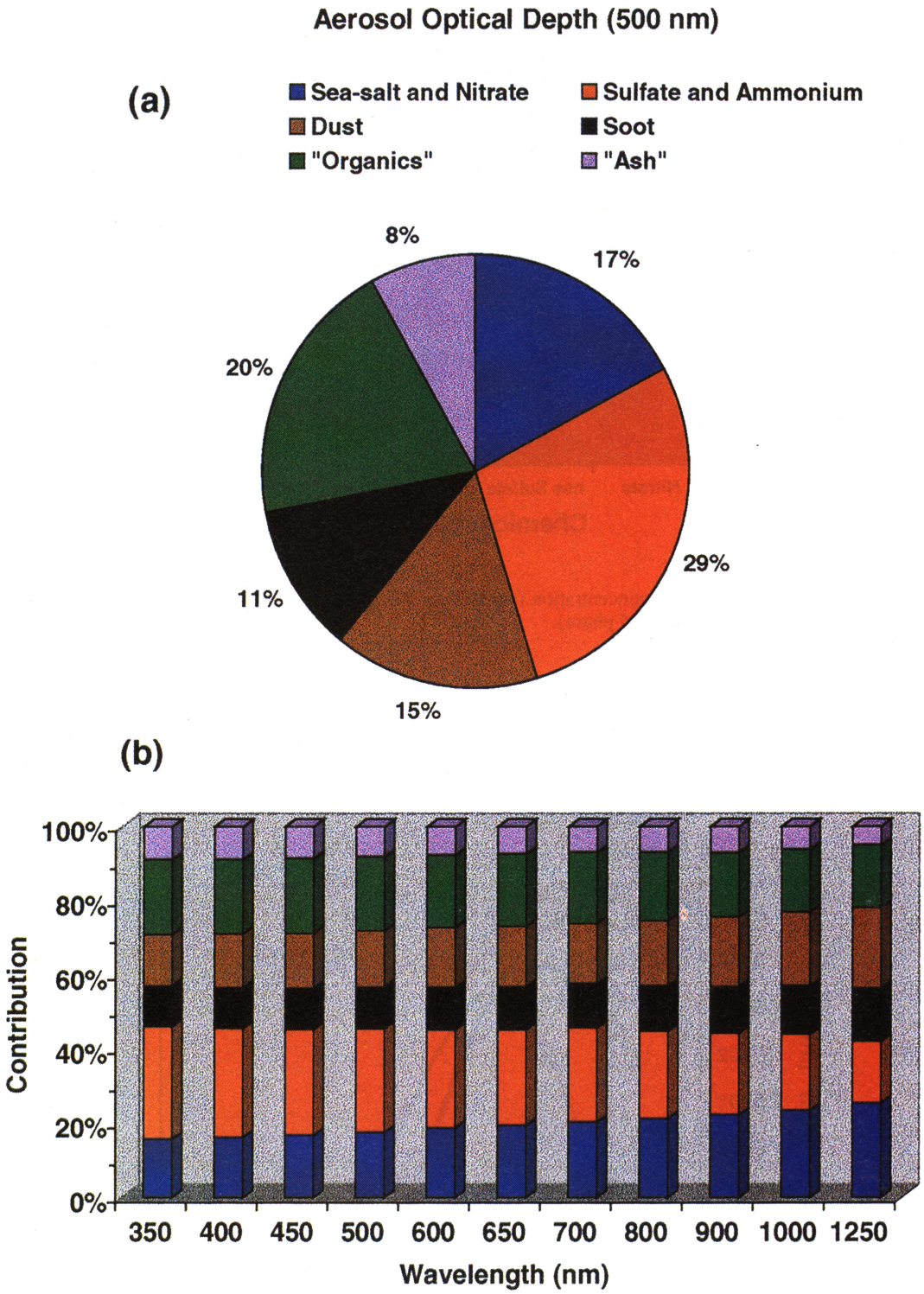


Plate 4(a). Relative contribution of various chemical species to the composite aerosol optical depth at 500 nm (estimated from the model). (b) Relative contribution of various chemical species to the composite aerosol optical depth as a function of wavelength.

assumed lognormal, given by (5). The total number concentration of aerosols is then adjusted to get a size distribution consistent with the measured aerosol mass concentration. As far as the aerosol system is concerned, soot is an important constituent that has very significant radiative effects in the atmosphere. At present the measurement of soot is unavailable at KCO. However, an estimate of the soot effect is obtained using the measured single-scattering albedo $\omega$ values obtained by an integrating nephelometer (measures aerosol scattering-coefficient) and a particle soot absorption photometer (aerosol absorption coefficient). The values of $\omega$ (after adjusting for humidity effects) indicate ranges from 0.88 to 0.90 [*Prospero et al.*, 1998]. The low values for the observed $\omega$ should not come as a surprise, given the amount of biomass burning, diesel vehicles, and two-stroke engines in the subcontinent. Without soot, the single-scattering albedo estimated for the composite aerosol system was 0.97. The soot concentration is increased in the composite aerosol system described above to make the single-scattering albedo 0.89. It is observed that ~6% by mass of soot are required for this purpose. The soot size distributions are also obtained following (4) using the mode radius and standard deviation for soot [*Hess et al.*, 1998].

At KCO, the size distribution of dust shows ~40% of the total dust mass in the submicron range. This is quite high compared with the mineral dust size distribution measured at other locations. For example, at Barbados, the submicron mineral dust is only ~15% of the total dust [*Li-Jones and Prospero*, 1998]. The high submicron dust fraction over the Indian Ocean could be due to the presence of submicron aerosols formed directly from biomass burning in the subcontinent. By examining the particle filter (in the PSAP), *Prospero et al.* [1998] found gray to dark gray coloration and suggested that the "mineral dust" component measured at KCO also consists of residues of biomass burning as well (could be a type of ash). This is also supported by the fact that coal is the largest naturally occurring source of conventional energy in India in many sectors, especially power, railways, cement, fertilizer, and domestic uses [*Basu and Chakrabarti*, 1990]. To separate the "ash" component from the mineral dust measured at KCO, we assumed that the size distribution of soil dust at KCO is similar to that measured at Barbados, since at both locations, dust was subject to long-range transport. By this assumption we found that most of the ash component is confined in the submicron range. The values of mode radii and standard deviation (at 75% RH) used for generating aerosol size distributions of individual species are given in Table 6.

The size distribution of different chemical species thus generated is shown in Plate 3. The details of the component "missing organics" will be explained in section 3.2.2.

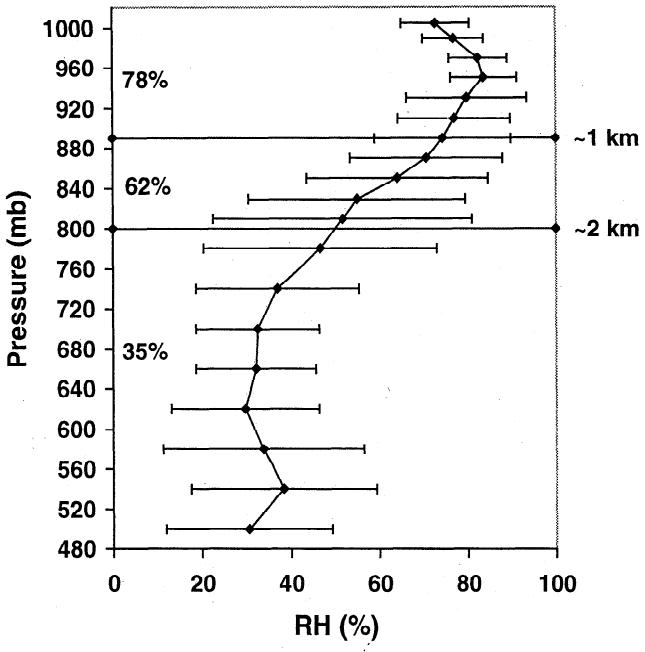


Figure 5. Vertical variation of relative humidity (average of eight profiles) inferred from sonde data (see text for details).

**3.2.2. Vertical distribution and columnar optical depths.** The spectral values of aerosol optical depths are estimated from the individual size distributions (which are consistent with the measured mass). Aerosols are assumed externally mixed. The extensive study of the sensitivity of aerosol direct forcing to aerosol size and chemical composition by *Pilinis et al.* [1995] has shown that the difference in the forcing for external and internal mixed aerosols is small.

The aerosol optical depths are estimated by assuming that the concentrations of all aerosol components are constant in the boundary layer (1 km) and then decrease exponentially with altitude with a scale height of 800 m (as inferred from the Lidar images). This assumption is also consistent with other field measurements [*Blanchard and Woodcock*, 1980]. The vertical profiles (average of approximately eight profiles) of RH obtained from the balloon sonde data (Figure 5) have revealed an increase in RH with altitude in the marine boundary layer followed by a decrease at higher altitudes. Under cloud-free conditions, RH did not show significant changes with altitude above ~2 km but remains more or less the same up to a height of ~8 km. In the present study, while computing columnar aerosol optical depth, the vertical changes due to RH have been taken into account by using three mean RH values (estimated from sonde data) for the

**Table 6.** Model Parameters of Aerosol Size Distribution

| Parameter/Aerosol Type | $r_m, \mu_m$ | $\log \sigma_m$ |
|---|---|---|
| Sea salt, accumulation mode | 0.416 | 0.307 |
| Sea salt, coarse mode | 3.49 | 0.307 |
| Dust, transported | 0.50 | 0.342 |
| Non-sea-salt sulfate and ammonium | 0.0306 | 0.350 |
| Soot | 0.0118 | 0.301 |
| "Ash" | 0.08 | 0.20 |

**Table 7.** Mean Aerosol Optical Depths at 500 nm for Various Species

| Species | $\tau_p$ |
|---|---|
| Sea-salt and nitrate | 0.034 |
| Dust | 0.030 |
| nss sulfate & ammonium | 0.055 |
| Soot | 0.022 |
| "Organics" | 0.039 |
| "Ash" | 0.016 |

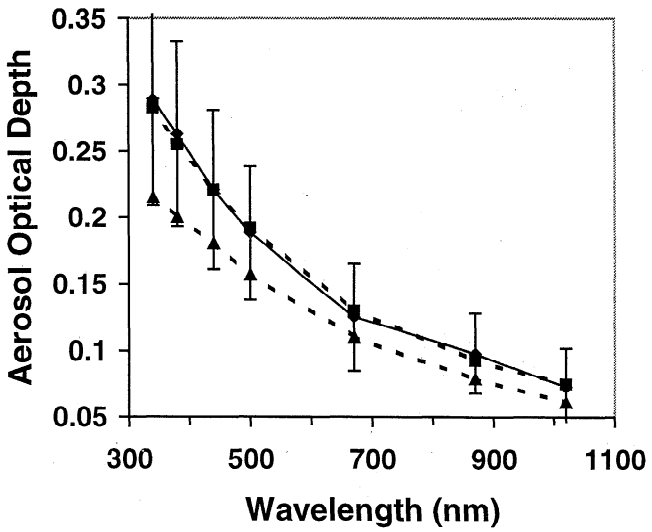


Figure 6. Comparison of estimated (dashed line and triangles) and measured (solid line and diamonds with vertical bars) aerosol spectral optical depths. Vertical bars represent standard deviations of the mean values. Also shown (dashed line with squares) are the spectral optical depths after addition of a new aerosol mode, which is attributed as organic aerosols (see text for details).

three altitude regimes. A mean value of 78% for the first 1 km, 62% for the altitude range from 1 to 2 km and 35% for altitudes above 2 km have been used. The sea-salt and non-sea-salt sulfate and ammonium are considered hygroscopic. Some of the investigators found the presence of a hydrophobic film over the aerosol particles, which inhibits the humidity growth [e.g., *Cantrell et al.,* 1997]. Owing to the lack of data, we are unable to discuss this aspect in detail at present. The estimated aerosol optical depths (for each of the chemical species considered here) are shown in Table 7. The complex refractive indices of each chemical species are taken from *Hess et al.* [1998]. However, the refractive index for ash component is not given by *Hess et al.* [1998], and values given by *Patterson* [1981] have been used.

The composite aerosol optical depth (i.e., the sum of optical depths due to the individual aerosol species) is compared with the mean value of the columnar optical depth measured with CIMEL during FFP and the results are plotted in Figure 6. The vertical bar represents the standard deviations of the mean values. It is clear that the model (Figure 6, dashed line with solid triangles) is missing some major factor (components). The missing aerosol could be either due to the presence of some other species (most likely organics) which are not retrieved from the filter samples or due to the presence of an aerosol layer above the marine boundary layer which obviously will not appear in the surface (in situ) measurement. The difference in optical depths, which show large values in the visible wavelengths compared to NIR wavelengths, suggests that the missing component has a significant submicron fraction. The deficit in the small aerosols is most likely due to organic aerosols (from biomass burning) that were not measured at KCO. By an iterative step, we added a small aerosol mode to match the spectral variation of the estimated aerosol optical depths with that revealed by CIMEL. The computed columnar optical depth with the addition of the missing aerosols is also shown (as dotted line) in Figure 6.

The relative contribution (RC) of each of the aerosol species to the total optical depth of the composite aerosol system is estimated as a function of $\lambda$. Semiempirical relations for the spectral dependence of the RC (separately for each aerosol species) are also developed, since that is important information for estimating the radiative fluxes. The wavelength dependence of RC is expressed in the form

$$RC_i(\lambda) = a_i + b_i * \lambda \quad (8)$$

where $\lambda$ is in μm and $i$ represents different chemical species. The percentage contribution in aerosol optical depth of each chemical species is shown in Plate 4a. The relative contribution varies slightly with wavelength, especially for sulfates and sea salt, as shown in Plate 4b. The coefficients $a_i$ and $b_i$ which define RC ($\lambda$) for each of the aerosol species, are given in Table 8.

## 4. Validation of the Aerosol Model: Comparison of Radiative Fluxes

The aerosol model described above has been used in a Monte Carlo radiative transfer model [*Podgorny et al.*, 1998, 1999] to estimate the broadband (0.2–4.0 μm) fluxes at the surface and the top of the atmosphere. A Monte Carlo radiative transfer model is used for the present study, because it allows us to treat each aerosol species explicitly in the model. The bands from 0.2 to 4.0 μm are divided into 38 narrow bands. The absorption due to water vapor and $CO_2$ are estimated by using exponential sum fitting of transmissions (ESFT) coefficients, and that due to $O_2$ and $O_3$ are estimated by using the corresponding spectral absorption coefficients [*Shi*, 1994]. The zenith-angle-dependent ocean albedo has been taken from *Breigleb et al.* [1986].

The cloud-screened values of spectral optical depths (obtained from CIMEL) are used to estimate the radiative fluxes. Each of the chemical species is treated separately in the Monte Carlo model by using the corresponding phase functions and single scattering-albedos for individual species [*Hess et al.*, 1998]. Since the sea salt and the component that consists of non-sea-salt sulfate and ammonium are hygrosopic in nature, different phase functions are used for the three altitude regimes described in section 3.2.2. The global, diffuse, direct, and TOA fluxes (for the bands corresponding to the pyranometer and pyrheliometer measurements) are estimated corresponding to each CIMEL observation and for the same zenith angle of measurement. The percentage contribution in aerosol optical depth of each of the chemical

**Table 8.** Coefficients Defining the Spectral Variation of Relative Contribution

| Aerosol Type | Coefficients | |
|---|---|---|
| | $a_I$ | $b_I$ |
| Sea salt | +11.8562 | +11.2937 |
| Dust | +10.8115 | +8.7873 |
| Non-sea-salt sulfates and ammonium | +35.5910 | -15.0870 |
| Soot | +9.2511 | +3.8787 |
| "Missing organics" | +22.1387 | –4.6981 |
| "Ash" | +10.3235 | -4.1774 |

**Table 9.** Comparison of Calibration Constants (Sensitivity)

| Radiometric Sensor | Kipp & Zonen, Manufacturer[a] $\mu V / W m^{-2}$ | NOAA CMDL, Recalibrated[b] $\mu V / W m^{-2}$ |
|---|---|---|
| Pyrheliometer (70148) | 11.73 | 11.76 |
| Pyranometer I (70395) | 13.58 | 13.82 |
| Pyranometer II (70396) | 12.06 | 12.16 |

[a] Purchased in July, 1997 and calibrated in the Kipp & Zonen labs in The Netherlands.

[b] Calibrations were carried out under clear skies in Boulder, CO in September, 1997 at the National Oceanic and Atmospheric Administration Climate Monitoring and Diagnostics Laboratory (by E. Dutton).

species is estimated according to (8). The columnar water vapor content for each day (estimated from the CIMEL measurements) has been used to estimate the water vapor absorption. An arbitrary water vapor profile is scaled to make the columnar water vapor content consistent with the daily measured values.

The calculated fluxes at the surface are compared with the corresponding fluxes measured by the pyranometers and the pyrheliometer; the fluxes at the top of the atmosphere are compared with Clouds and Earth's Radiant Energy System (CERES) [*Wielicki et al.*, 1996].

### 4.1. Surface Radiometers

The Kipp & Zonen pyrheliometer measures the normal solar irradiance, i.e., the direct solar radiation normal to the plane of incidence. The manufacturer-specified absolute accuracy (zero offset) of this instrument is ±3 W $m^{-2}$ with a stability (precision) of ~1% $y^{-1}$. In addition to the pyrheliometer, we deployed two broadband ventilated Kipp & Zonen pyranometers, one shaded from the direct beam to measure the diffuse radiation and a second, unshaded instrument which measures the total (direct and diffuse) radiation. The pyranometers have an absolute accuracy (zero offset) of ~± 9 W $m^{-2}$. In addition, the error due to directional response (that is the detector responds differently to radiation depending on the incident angle) can be as much as ±10W$m^{-2}$. The shaded pyranometer and the pyrheliometer are mounted on Sun trackers. When comparing the diffuse fluxes measured by the shaded instrument, we account for the effects of the shading arm and ball. The combined effect of the arm and the ball is to decrease the diffuse flux by ~9 W $m^{-2}$ for overhead Sun and ~4 W $m^{-2}$ for horizon Sun.

In summary, we have two independent methods for determining the global radiation (or the irradiance): (1) direct solar radiation (pyrheliometer value multiplied by cosine of the solar zenith angle) plus diffuse radiation (the shaded pyranometer) and (2) global radiation by the unshaded instrument. However, since the pyrheliometer accuracy is better than the pyranometer by at least a factor of 2 and since the pyrheliometer does not have to contend with angular response (it is always facing normal to the solar incidence plane), method 1 is used here for global radiation. All three of the instruments were calibrated (before deployment) at the calibration facility at NOAA CMDL (by E. Dutton), and the calibration constants (see Table 9) were within 1% of that given by the manufacturer.

### 4.2. CERES TOA Albedos

The Clouds and Earth's Radiant Energy System radiometer is perhaps the best broadband radiometer flown in space, with an absolute accuracy of 0.2% or better and comparable precision. CERES was launched in December 1997 and is calibrated during prelaunch and routinely during orbit using in-flight calibration sources [*Lee et al.*, 1999]. Calibration of the instrument (instrument gain) has changed by <0.1% in 9 months of space flight. CERES measures the radiance, which is then converted to irradiances (fluxes) using empirical algorithms [*Wielicki et al.*, 1996]. As a result, the irradiances are subject to larger uncertainties (than the radiances). With respect to the present study, it should be noted that the least uncertainty in these algorithms is shown to be for clear-sky oceanic regions [e.g., see *Ramanathan et al.*, 1989], which are the only cases considered in this study.

A comparison of the surface fluxes is shown in Plates 5a-c. Since soot was not directly measured at KCO (but inferred from the single scattering albedo measurement), we show two cases: with and without soot. We had to make one modification to the model. The observations cover the wavelength region of 0.29 to 2.8 μm, while the model includes 0.2 to 4 μm. For the results shown in Plate 5, we have changed the model spectral region to correspond with observations. For all three cases (direct, diffuse, and global), the soot model is in much better agreement. It should be kept in mind that most of the flux variations (e.g., the 400 to 1000 W $m^{-2}$ ranges in Plate 5a) are due to variation in the solar zenith angle (time of day).

For the direct flux, both the slope and the offset (mean error) for the with-soot model agree within 0.3%, i.e., within the pyrheliometer uncertainty. The offset for the without-soot model is larger by about a factor of 4. For the diffuse flux the slope is within 1% of perfect agreement (for both the with- and without-soot models), but the offset is twice as large for the without-soot model, although the offset for both models agrees within the instrumental uncertainty of 7 W $m^{-2}$. For the global flux the with-soot model is in near-perfect agreement for both the slope and the offset, while the offset for the without soot model is as much as 17 W $m^{-2}$. This should not be a surprise, since the measured single-scattering albedo is ~0.9 and without soot, the single-scattering albedo is significantly larger. The excellent agreement shown in Plate 5a provides strong validation for the aerosol model (including soot) presented here. The surprising success of this validation process is due to the combination of the following factors: (1) We eliminated one of the largest sources of errors in clear-sky models, i.e., specification of aerosol properties consistent with aerosol data. (2) Our comparison is done statistically with a large number of independent samples, as opposed to a case-by-case study of comparison of individual fluxes. (3) We eliminated one of the biggest uncertainties in radiometric measurements by adopting method 1 as opposed to method 2, which uses the unshaded pyranometer for the global flux. For example, in Figure 7, we compare the global flux measured through method 1 with that of method 2. There is a large

offset of ~17 W $m^{-2}$ (3%), and the slope is ~2.5% off from the perfect slope of 1. The basis for choosing method 1 as a superior one is as follows:

First, the pyrheliometer absolute accuracy is a factor of 3 better (3 W $m^{-2}$ versus 7 to 10 W $m^{-2}$). Since the direct flux is about a factor of 5 larger than the diffuse (compare Plate 5a with 5b), minimizing the error in the direct flux is highly preferable. Second, the largest source of error in the unshaded global pyranometer measurement is the angular response error to direct solar radiation (simply because direct solar is the dominate term in the global irradiance, and it changes significantly from morning to evening); method 1 does not suffer from this error, because the pyrheliometer is a normal incidence radiometer. The mean differences and root-mean-square differences between the estimated and measured fluxes are shown in Table 10 where the values given for the global flux correspond to method 1.

We now compare the TOA clear-sky albedo from CERES with the model results for KCO. Note first that CERES has a low inclination orbit, and we get only one daytime measurement over the Arabian Sea; the pixel size varies from ~10 km (for nadir) to ~30 km for slant viewing angle (say, 60°). The following criteria were used to select the CERES data: the time of CERES clear sky measurement should match the time of KCO clear-sky data within 15 min, and the spatial location of CERES clear-sky pixel should be within 25 km of KCO. Figure 8a shows the CERES TOA albedo along with the model values as a function of the day (counted from January 1). Figure 8b panel shows the solar and satellite zenith angle for the times of data collection. The data and model albedos agree excellently (within ~0.005) when the solar and satellite angles are less than 50° (examine Figures 8a and 8b), and for the few data points when these angles exceed 50° (slant angles), the differences exceed 0.03. We propose the following reasons for the larger difference for the slant angles: first, the algorithms for converting satellite radiances to fluxes are particularly prone to errors for slant solar and viewing angles; and second, cloud contamination of scenes is more likely for slant satellite viewing angles (note that there is a systematic difference, with CERES albedos always larger for the slant angles). In summary, the model is in excellent agreement with the observed fluxes at the surface and at the TOA.

## 5. Discussion

The Indian Ocean region is a data sparse region, and hence it is important to compare the present results with others reported in the literature.

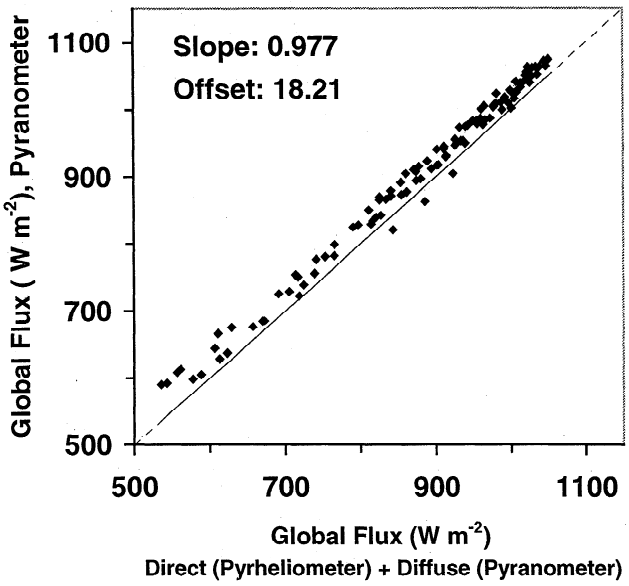


Figure 7. The comparison of global flux obtained by the two methods 1 and 2 described in the text.

### 5.1. Comparison with Other Oceanic Regions

A comparison of the scattering coefficients (obtained by nephelometers) can be seen in Table 11. The values of the scattering coefficient estimated for the tropical Indian Ocean seem to be higher compared with those for other sites, including the coastal site at Washington. This perhaps is due to a combination of the significant influence of emissions from the subcontinent and the confinement of the aerosols in the boundary layer (see Plate 1), both of which will enhance the near-surface scattering coefficient. A comparison of the mass-scattering efficiencies of sulfate aerosol is shown in Table 12, where many of the values are taken from *Charlson et al.* [1999]. The present value of 4.43 $m^2$ $g^{-1}$ is well within the range of observed values in the literature.

Table 13 compares the time mean aerosol optical depths for the individual species (for dust, sulfate, sea salt, and carbonaceous aerosols) estimated from the present study (average for February 20 to March 31), with the monthly mean values (for February and March) of Arabian sea optical depths estimated by *Tegen et al.* [1997, Figure 5c] for the Arabian Sea using a global transport model. It should be noted that Tegen et al.'s values are for the northern Arabian Sea (10°N to 25°N), whereas the present values are for the southern Arabian Sea (4°N). The agreement between the

**Table 10.** Mean Difference and Root Mean Square Difference Between Estimated and Measured Fluxes at the Surface

| Flux | With Soot | | Without Soot | |
|---|---|---|---|---|
| | Mean Difference | RMS Difference | Mean Difference | RMS Difference |
| Direct | -3.61 | 4.25 | 4.39 | 4.93 |
| Diffuse | -6.19 | 14.81 | 3.29 | 11.66 |
| Global | 7.01 | 10.10 | 15.07 | 18.36 |

model and the measured values is excellent for sulfate and carbonaceous aerosols. The dust optical depth, on the other hand, differs by a factor of 2. This is most likely due to the fact that the northern Arabian sea is closer to the dust source (north Africa and the Rajasthan desert) than KCO. In fact, the dust optical depth inferred from this study agrees better with the global average values reported by *Tegen et al.* [1997].

### 5.2. Factors Governing the Mean and Variance of Aerosol Optical Depths

Up to this point, we have ignored the factors that determine the daily variations in the optical depths, which we will consider now. The daily variability ($\tau_{pmax}$–$\tau_{pmin}$) in the CIMEL measured $\tau_p$ during FFP is 0.21 (Figure 3). The processes affecting the aerosol characteristics over this region are (1) sea surface wind speed, (2) relative humidity, and (3) the transport of aerosols from nearby continents.

The relative effect of wind speed and RH are examined first using the respective indices (see section 3 for the dependence of $\tau_p$ with wind speed and relative humidity), and the rest is attributed to those aerosols transported from the continents. The aerosol production due to wind speed is accounted for by (2) in conjunction with wind speed data shown in Figure 1. The wind speed ranges from ~1.5 m $s^{-1}$ to 7 m $s^{-1}$ and (2) yields variation in $\tau_v$ of 0.025, which is ~12% of the 0.21 range in $\tau_v$ (Figure 3). This is consistent with the 14% variability in the measured concentration of sea salt.

In a similar way, the maximum variability in $\tau_p$ caused by RH variation from 66% to 77% (Figure 2) during the FFP is estimated to be 43% (from the relation $\delta\tau = 0.0083\ \delta RH$; see section 3.1). Thus wind speed and relative humidity can account for only 55% of the total variation; the balance of

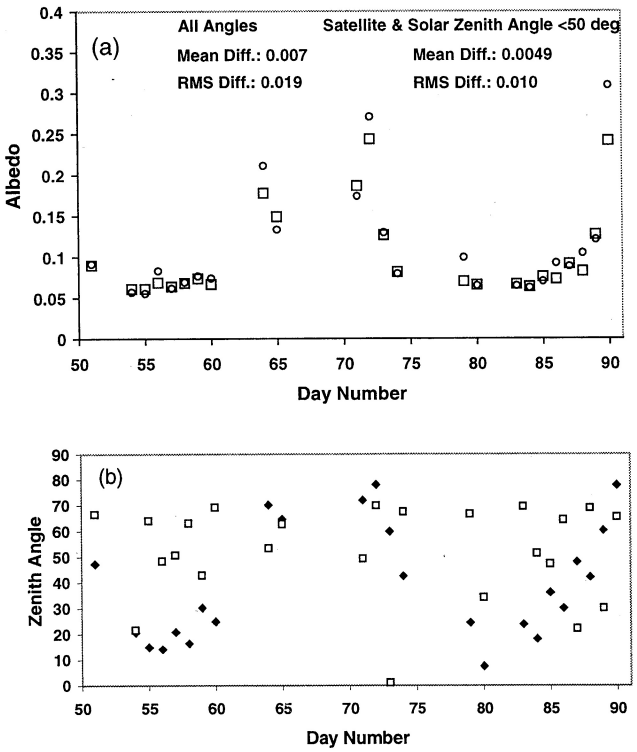


Figure 8. Comparison of the top of the atmosphere fluxes (estimated using Monte Carlo radiative transfer model (squares) and those measured with the CERES satellite). (b) Solar (diamonds) and satellite (squares) zenith angles at times of collection.

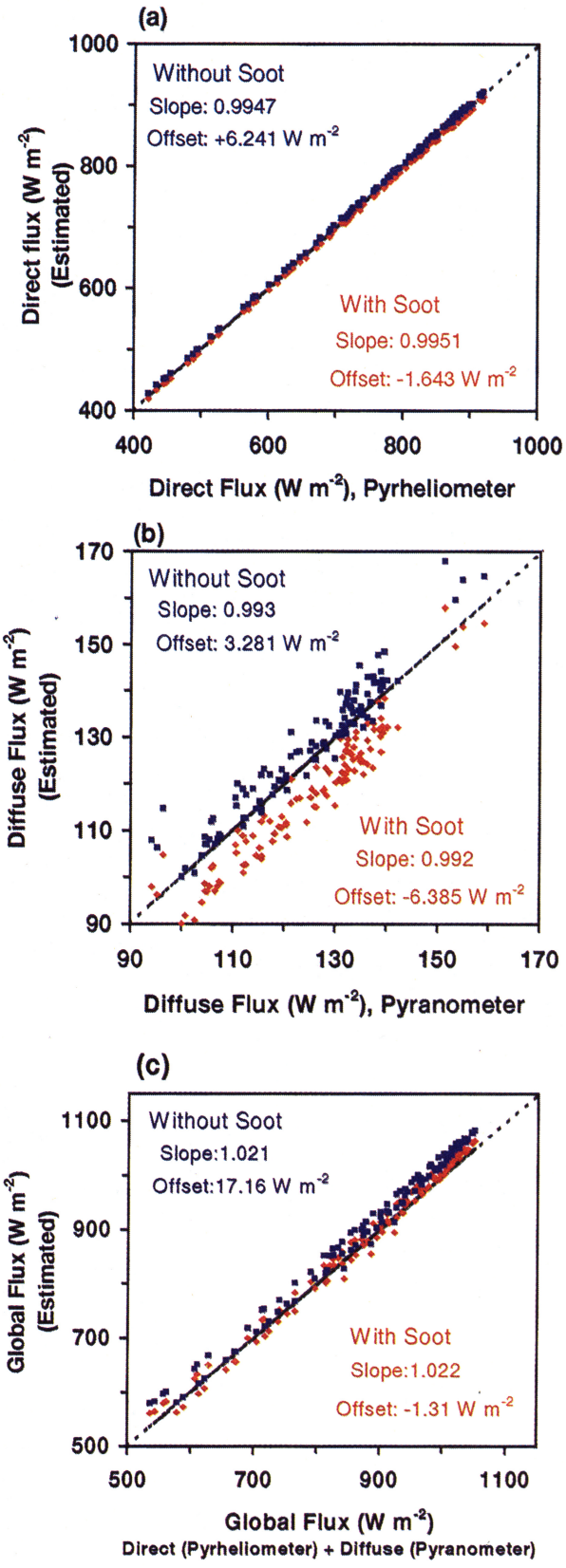


Plate 5. Comparison of measured and estimated surface (a) direct (b) diffuse, and (3) gloal fluxes (see text for details).

**Table 11.** Comparison of Scattering Coefficients

| Instrument | Scattering Coefficient ($10^{-6}$), $m^{-1}$ | Location | Reference |
|---|---|---|---|
| Forward Scattering Spectrometer Probe (PSSP-300), Thermo Systems, Inc. | 17–31 | Remote Southern hemisphere marine boundary layer | *Baumgardner and Clarke* [1998] |
| Three-wavelength nephelometer, TSI, Inc. | 4.4±3.0 ($D$<1 μm)<br>23±16 (1 μm<$D$<10 μm) | Southern Ocean near Australia | *Quinn et al.* [1998] |
| Integrating nephelometer | 9.8–15 | Pacific Ocean | *Quinn et al.* [1995] |
| Integrating nephelometer | 3.7–14.0 | Cheeka Peak, Washington coast | *Quinn et al.* [1995] |
| Integrating nephelometer | 26.9±28.3 | Continental location at Illinois | *Shrestha* [1996] |
| Controlled RH nephelometery | 15.4±7.9 | Cape Grim, Tasmania | *Carrico et al.* [1998] |
| Nephelometer, Radiance Research, Inc. | 44.73±13.08 ($D$<10 μm)<br>25.03±7.6 ($D$ <1μm) | tropical Indian Ocean | Present Study |
| Estimated from model | 51.07 ($D$<10 μm)<br>31.29 ($D$ <1μm) | tropical Indian Ocean | Present Study |

Here $D$ is the aerosol diameter

45% must be due to variations in the transport of dust and other continental aerosols. Estimation of the effect of the changes in dust concentration has shown that it can cause changes in $\tau_v$ up to 23%. The changes in the concentration of the non-sea-salt sulfate and ammonium are observed to be 15%, and the balance of ~7% can easily be accounted for by organics and other carbonaceous aerosols (not measured at KCO).

### 5.3. Anthropogenic Contribution to Mean Optical Depth

The contribution of the various species to the observed optical depth is shown in Plate 4a. Here we make an attempt to differentiate between natural and anthropogenic sources. In remote marine location like Kaashidhoo, the only natural sources of aerosols are the production of sea salt, dust transported by winds, and nss sulfate aerosols formed by gas-to-particle conversion processes, the precursor gases being those emitted from the ocean (e.g., DMS).

Sea salt contributes 17% to $\tau_v$ (Plate 4a); dust (assuming that all of it is natural) contributes another 15%. The nss sulfate can have both natural and anthropogenic sources. Measurements of methane sulfonic acid (MSA) from an earlier cruise in the Arabian Sea [*Krishnamurti et al.*, 1998] reveal the DMS source for the observed sulfate to be very small, <20%. The measurements of each species at KCO have shown that the amount of sulfate is ~3 times that of ammonium. Thus out of the 29% for sulfate and ammonium, sulfate (DMS and anthropogenic) contribution is ~20%. If 20% of this sulfate is from natural sources (and the balance from industrial pollution from transport), we estimate that the natural source of sulfate contributes ~4% to $\tau_v$. Since we have used the upper estimate for natural sources, the overall contribution of natural sources is <36%(17+15+4). Thus anthropogenic contribution to the total aerosol optical depth is >64%.

### 5.4. Ratio of Soot to Organic Matter

The ratio of soot (black carbon) to organic matter content is an indicator of the source of absorbing aerosols [*Mcdow et al.*, 1996]. A comparison of the ratio of black carbon to

**Table 12.** Comparison of Sulfate Mass Scattering Efficiencies

| $\alpha SO_4^=$, $m^2 g^{-1}$ | RH, % | Wavelength, nm | Empirical Approach | Reference |
|---|---|---|---|---|
| 5 ± 2 | < 50 | 530 | univariate regression of $SO_4^=$ with light scattering | *Waggoner et al.* [1976] |
| 6.6 ± 0.4 | 40 - 50 | 525 | bivariate regression of $SO_4^=$ and organic carbon with light scattering | *White* [1990] |
| 5 ± 2 | 50 | 530 | based on *Waggoner et al.* [1976] | *Charlson et al.* [1991, 1992] |
| 2.84 ± 0.14 | < 40 | 550 | regression of light scattering on total submicron mass | *Hegg et al.* [1993] |
| 3.6 ± 1.1 | 30 | 550 | multivariate regression of measured light scattering on submicron and supermicron component masses | *Quinn et al.* [1995] |
| 4.3 – 7.5 | 30 | 550 | Multivariate regression of measured light scattering on submicron and supermicron component masses | *Quinn et al.* [1996] |
| 5 | 30 | 550 | model | *Kiehl and Breigleb* [1993] |
| 4.43 | < 40 | 530 | model | Present study |

**Table 13.** Comparison of Aerosol Optical Depths

| Location/ Species | Sea-salt | Dust | Sulfate | Carbonaceous, Organics+BC | Reference |
|---|---|---|---|---|---|
| Global mean | 0.007 | 0.029 | 0.025 | 0.019 | *Tegen et al.* [1997, Table 1] |
| Arabian Sea | 0.01 | 0.07 | 0.035 | 0.055 | *Tegen et al.* [1997, Figure 5(c)] |
| Tropical Indian Ocean | 0.023 | 0.030 | 0.037 | 0.061 | present Study |

organic matter estimated from the present aerosol model with that for different types of sources is shown in Table 14. The highest values, from ~0.5 to 4, are found in urban regions and in diesel exhaust, where the elemental carbon mass is ~4 times the organic matter. As the particles age in the atmosphere, the organic matter in relation to elemental carbon increases because of photochemical processes [*Mcdow et al.*, 1996]. As such, the value of 0.422 estimated in the present study suggests that the absorbing aerosol source which is influencing the tropical Indian Ocean regions is mainly urban pollution including diesel exhaust.

### 5.5. Effect of Mixing State

The model, thus far, assumes that the different aerosol species are externally mixed. The sensitivity of the mixing state of aerosols to the optical and radiative properties is examined briefly in this section. We now will make the other extreme assumption, i.e., that all of the aerosol species are internally mixed. For this purpose a combined size distribution is used for an internally mixed aerosol system. The volume-weighted refractive index and single-scattering albedos are used to estimate the optical and radiative properties. Estimated aerosol optical depth showed ~1% decrease when compared with the externally mixed case. The total aerosol number density is slightly adjusted to make the estimated aerosol optical depth (for internally mixed aerosols) consistent with that observed by the Sun photometer (CIMEL). In the Monte Carlo radiative transfer model, the complete aerosol system is treated as a single component instead of separate as individual species as in the case of externally mixed aerosols. The global fluxes from the two aerosol models agree within 0.5%. The maximum difference of ~3 W $m^{-2}$ was observed for overhead Sun for both the global and the diffuse fluxes. Apparently, the mixing state of aerosols does not change any of our conclusions.

## 6. Conclusions

As a part of INDOEX, a new observatory has been established by $C^4$ for the measurement of aerosols and radiation over the tropical Indian Ocean, which is an ideal site for estimating the global influence of the subcontinent [*Krishnamurti et al.*, 1998]. Extensive measurements of aerosol chemical, physical, and optical properties simultaneous with measurements of radiative fluxes at the ground as well as at the top of the atmosphere during the INDOEX FFP 1998 have enabled us to develop an aerosol model for the tropical Indian Ocean that is consistent with measurements. The primary findings of this study are summarized as follows;

(1) The major factors affecting the aerosol characteristics over the tropical Indian Ocean during the northeast monsoon period are the transport of pollutants from the Asian subcontinent and, to a lesser extent, the changes in RH. Surface winds observed are low, and therefore the direct aerosol production at the sea surface is not an efficient production mechanism. Anthropogenic sources contribute as much as 65% to the observed optical depths.

(2) At this remote island the visible aerosol optical depths reach values as high as 0.4, with monthly means of ~0.2.

(3) The Angstrom wavelength exponent is found higher (almost double) compared to the earlier measurements over oceanic regions and is comparable with that measured near the coastal regions of the Indian subcontinent.

(4) The aerosol size distributions retrieved from measurements of spectral optical depths shows bimodal characteristics, with a primary small-particle mode at ~0.135 μm and a secondary large-particle mode at ~0.955 μm radius.

(5) The large variability in aerosol optical depths observed is attributed equally to the variability in the transport pattern, which carries air masses of different origin, and the changes in the RH.

(6) A detailed aerosol model has been developed that includes the effects of sea salt, sulfates, dust, soot, organics, fly ash, nitrates, and ammonium.

(7) The discrepancy between the spectral aerosol optical depths estimated from the surface measurements (making use of the lidar images for the vertical aerosol profile) and those measured simultaneously with the CIMEL radiometer is attributed to the components that are not included in the

**Table 14.** Ratio of Elemental Carbon to Organic Matter

| Source | Elemental Carbon/ Organic matter | Reference |
|---|---|---|
| Diesel exhaust | ~4.0 | *Japar et al.* [1984] |
| | ~1.25 | *Hildemann et al.* [1991] |
| Wood smoke | ~0.05–0.10 | *Rau* [1987] |
| | ~0.059 | *Hildemann et al.* [1991] |
| Urban pollution | ~0.5–0.67 | *Shah et al.* [1986] |
| Smog | ~0.2–0.25 | *Turpin et al.* [1991] |
| Over tropical Indian Ocean | 0.422 | Present study |

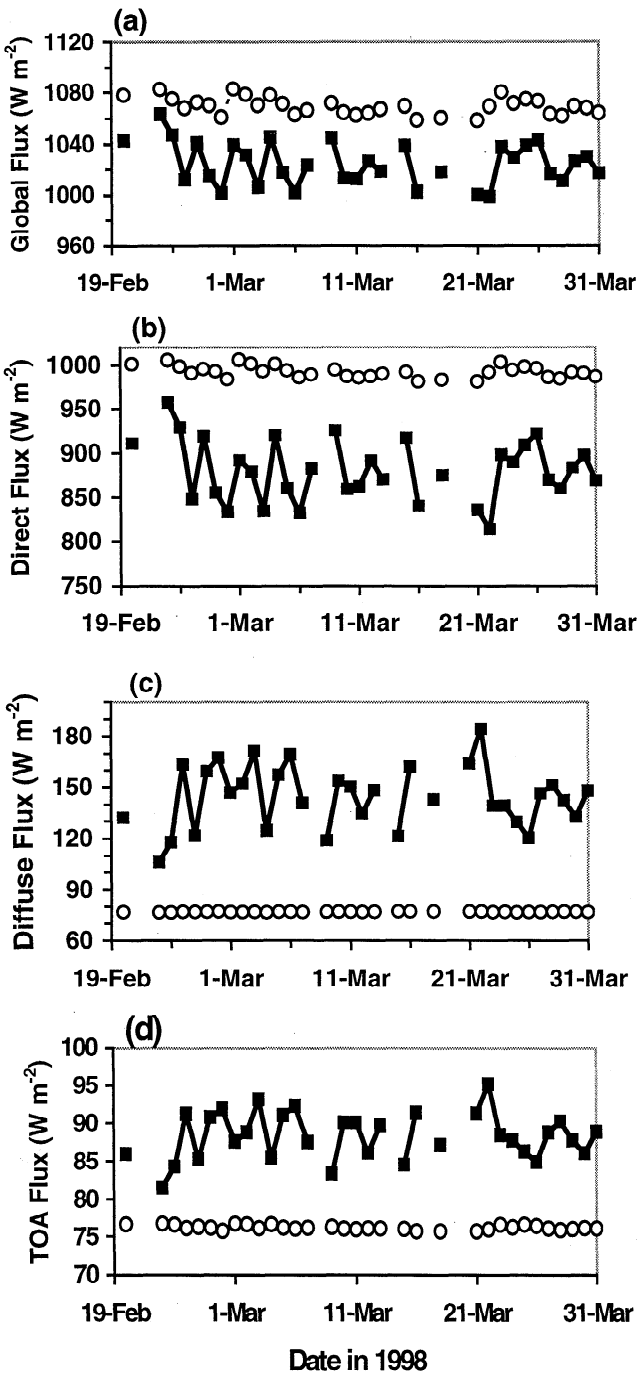


Figure 9. Estimated fluxes corresponding to the daily mean CIMEL-measured aerosol optical depths with aerosols (squares) and without aerosols (circles), (a) global flux, (b) direct flux, (c) diffuse flux, and (d) TOA flux.

surface measurements. These include organics, soot, and fly ash.

(8) Aerosol single-scattering albedo is observed as ~0.90 which suggests the presence of absorbing aerosols. The surface-scattering coefficient is in the upper range of those observed for oceanic regions, thus indicating the high aerosol content of the boundary layer in the tropical Indian Ocean.

(9) A comparison of the ratio of elemental carbon to organic matter with that associated with different sources of carbonaceous aerosols indicates that the sources of these aerosols are most likely diesel exhaust and urban pollution including biomass burning.

(10) The aerosol model, when incorporated in a radiation model, generates radiation fluxes that are in excellent agreement (within a few percent) with measured surface fluxes and TOA albedos. In particular, the agreement with the direct and diffuse solar fluxes (<2%) provides a strong confirmation of the comprehensive aerosol model proposed here.

The next important step is to estimate the aerosol radiative forcing. To indicate the significance of this issue, we show in Figure 9, the fluxes computed by the model, at the surface and the TOA, with and without aerosols. The global fluxes decrease by as much as 50 to 80 W $m^{-2}$, the diffuse flux increases by as much as 60 to 90 W $m^{-2}$ and the TOA fluxes increase by as much as 15 W $m^{-2}$ (all fluxes for overhead Sun estimated using the daily mean aerosol optical depth and columnar water vapor content). Clearly, the aerosols transported from the subcontinent can have a large impact on the tropical Indian Ocean. To make further progress, we need more information from aircraft, which is expected to provide the vertical profiles for the absorption coefficient and aerosol size distribution, the subject of the intensive field phase of INDOEX to be conducted during January to April 1999.

**Acknowledgments.** We are indebted to the Government of Maldives for providing the land for KCO and for much assistance during every part of the KCO development and operation, with special thanks to the Ministry of Environment and Planning. We thank Hung Nguyen, who manages this facility. We thank A. Heymsfield and Craig Walther for organizing the lidar deployment. We would like to thank C. Venkataraman for useful discussions on the fly ash. The authors thank the National Science Foundation (NSF) for funding the KCO observatory through grant ATM 9612887, NASA for funding the CIMEL and CERES portions of this study, and the Department of Energy for funding portions of the Monte Carlo model study through the ARM program. This is INDOEX publication 24 and publication 207 of the Center for Clouds, Chemistry and Climate. We thank one of the anonymous reviewers and R.J.Charlson for their valuable comments.

## References

Andreae, M.O., Climatic effects of changing atmospheric aerosol levels in *World Survey of Climatology*, vol. 16, *Future Climates of the World*, edited by A. Henderson-Sellers, pp. 341-392, Elsevier, New York, 1995.

Basu, C.K., and R.K. Chakrabarti, Optimal utilization of coal reserves, *Fuel Sci. Technol., 9*, 47-58, 1990.

Baumgardner, D., and A. Clarke, Changes in aerosol properties with relative humidity in the remote southern marine boundary layer, *J. Geophys. Res., 103*, 16,525-16,534, 1998.

Blanchard, D.C., and A.H. Woodcock, The production, concentration, and vertical distribution of sea salt aerosol, *Ann. N. Y. Acad. Sci., 338*, 330-347, 1980.

Box, M.A., and A. Deepak, Retrieval of aerosol size distributions by inversion of simulated aureole data in the presence of multiple scattering, *Appl. Opt., 18*, 1376-1382, 1979.

Breigleb, B.P., P. Minnis, V. Ramanathan, and E. Harrison, Comparison of regional clear-sky albedos inferred from satellite observations and model computations, *J. Clim. Appl. Meteorol., 25*, 214-226, 1986.

Cantrell, W., G. Shaw, R. Benner, and D. Veazey, Evidence for sulfuric acid coated particles in the Arctic air mass, *Geophys. Res. Lett., 24*, 3005-3008, 1997.

Carrico, C.M., M.J. Rood, and J.A. Ogren, Aerosol light scattering properties at Cape Grim, Tasmania, during the First Aerosol

Characterization Experiment (ACE 1), *J. Geophys. Res., 103*, 16,565-16,574, 1998.

Charlson, R.J., J.E. Lovelock, M.O. Andrea, and S.G. Warren, Oceanic phytoplankton, atmospheric sulfur, cloud albedo and climate, *Nature, 326*, 655-661, 1987.

Charlson, R.J., J. Langner, H. Rodhe, C.B. Leovy, and S.G. Warren, Perturbation of the Northern Hemisphere radiative balance by backscattering from anthropogenic sulfate aerosols, *Tellus, Ser.B*, 152-163, 1991.

Charlson, R.J., S.E. Schwartz, J.M. Hales, R.D. Cess, J.A. Coakley, J.E. Hansen, and D.J. Hoffmann, Climate forcing by anthropogenic aerosols, *Science, 255*, 423-430, 1992.

Charlson, R.J., T.L. Anderson, and H. Rodhe, Direct climate forcing by anthropogenic aerosols: Quantifying the link between atmospheric sulfate and radiation, *Contrib. Atmos. Phys., 72*(1), 79-94, 1999.

Crutzen, P.J., and M.O. Andreae, Biomass burning in the tropics: Impact on atmospheric chemistry and biogeochemical cycles, *Science, 250*, 1669-1678, 1990.

d'Almeda, G.A., P. Koepke, and E.P. Shettle, *Atmospheric Aerosols-Global Climatology and Radiative Characteristics*, A. Deepak, Hampton, Va., 1991.

Hanel, G., The properties of atmospheric aerosol particles as functions of the relative humidity at thermodynamic equilibrium with the surrounding moist air, *Adv. Geophys., 19*, 73-188, 1976.

Hansen, J.E., M. Sato, A. Lacis, R. Ruedy, I. Tegen, and E. Matthews, Climate forcings in the Industrial era, *Proc. Natl. Acad. Sci., U.S.A.*, 12,753-12,758, 1998.

Hegg, D.A., R.J. Ferek, and P.V. Hobbs, Light scattering and cloud condensation nucleus activity of sulfate aerosol measured over the northeast Atlantic Ocean, *J. Geophys. Res., 98*, 14,887-14,894, 1993.

Hess, M., P. Koepke, and I. Schult, Optical properties of aerosols and clouds: The software package OPAC, *Bull. of Am. Meteorol. Soc., 79*, 831-844, 1998.

Hildemann, L.M., G.R. Markowski, and G.R. Cass, Chemical composition of emissions from urban sources of fine organic aerosols, *Environ. Sci. Technol., 25*, 744-759, 1991.

Holben, B.N., et al., AERONET-A federated instrument network and data archive for aerosol characterization, *Remote Sens. Environ., 66*, 1-16, 1998.

Hoppel, W.A., J.W. Fitzgerald, G.M. Frick, and R.E. Larson, Aerosol size distribution and optical properties found in the marine boundary layer over the Atlantic Ocean, *J. Geophys. Res., 95*, 3659-3686, 1990.

Hoppel, W.A., G.M. Frick, J.W. Fitzgerald, and R.E. Larson, Marine boundary layer measurements of a new particle formation and the effects of non-precipitating clouds have on aerosol size distribution, *J. Geophys. Res., 99*, 14,433-14,459, 1994.

Jaenicke, R., *Tropospheric aerosol in Aerosol Cloud Climate Interactions*, edited by P.V. Hobbs, Academic, San Diego, Calif., 1993.

Japar, S.M., A.C. Szkarlat, R.A. Gorse, E.K. Heyerdahl, R.L. Johnson, J.A. Rau, and J.J. Huntzicker, Comparison of solvent extraction and thermal-optical carbon analysis methods: Applications to diesel vehicle exhaust, *Environ. Sci. Technol., 18*, 231-234, 1984.

Jayaraman, A., A.D. Lubin, S. Ramachandran, V. Ramanathan, E. Woodbridge, W. Collins, and K.S. Zalpuri, Direct observations of aerosol radiative forcing over the tropical Indian Ocean during the Jan.-Feb. 1996 pre-INDOEX cruise, *J. Geophys. Res., 103*, 13,827-13,836, 1998.

Jorge, H.G., and J.A. Ogren, Sensitivity of retrieved aerosol properties to assumptions in the inversion of spectral optical depths, *J. Atmos. Sci., 53*, 3669-3683, 1996.

Kaufman, Y.J., C.J. Tucker, and I. Fung, Remote sensing of biomass burning in the tropics, *J. Geophys. Res., 95*, 9927-9937, 1990.

Kiehl, J.T., and B.P. Breigleb, The radiative roles of sulfate aerosols and green house gases in climate forcing, *Science, 260*, 311-314, 1993.

King, M.D., Sensitivity of constrained linear inversion to the selection of Lagrange multiplier, *J. Atmos. Sci., 39*, 1356-1369, 1982.

King, M.D., D.M. Byrne, B.M. Herman, and J.A. Reagan, Aerosol size distributions obtained by inversion of spectral optical depths measurements, *J. Atmos. Sci., 35*, 2153-2167, 1978.

Krishnamurti, T.N., B. Jha, J.M. Prospero, A. Jayaraman, and V. Ramanathan, Aerosol and pollutant transport and their impact on radiative forcing over tropical Indian Ocean during the January-February, 1996 pre-INDOEX cruise, *Tellus, Ser.B, 50*, 521-542, 1998.

Kristament, I.S., J.B. Liley, and M.J. Harvey, Aerosol variability in the vertical in the southwest Pacific, *J. Geophys. Res., 98*, 7129-7139, 1993.

Kulkarni, M.R., B.B. Adiga, R.K. Kapoor, and V.V. Shirvaikar, Sea salt in coastal air and its deposition on porcelain insulators, *J. Appl. Meteorol., 21*, 350-354, 1982.

Lee, R.B., III, et al., Pre-launch calibrations of the clouds and Earth's radiant energy system (CERES) Tropical Rainfall Measuring Mission and Earth Observing System (EOS): Morning (AM-1) spacecraft thermistor bolometer sensors, *IEEE Trans. Geosci. and Remote Sens., in press*, 1999.

Li-Jones, X., and J.M. Prospero, Variations in the size distribution of non sea-salt aerosols in the marine boundary layer at Barbados: Impact of African dust, *J. Geophys. Res., 103*, 16,073-16,084, 1998.

Medow, S.R., M. Jang, Y. Hong, and R.M. Kamens, An approach to studying the effect of organic composition on atmospheric aerosol photochemistry, *J. Geophys. Res., 101*, 19,593-19,600, 1996.

Moorthy, K.K., S.K. Satheesh, and B.V. Krishna Murthy, Characteristics of spectral optical depths and size distributions of aerosols over tropical oceanic regions, *J. Atmos. Sol. Terr. Phys.*, 60(10), 981-992, 1998.

O'Dowd, C.D., and M.H. Smith, Physicochemical properties of aerosols over the northeast Atlantic: Evidence for wind speed related submicron sea-salt aerosol production, *J. Geophys. Res., 98*, 1137-1149, 1993.

Patterson, E.M., Measurements of the imaginary part of the refractive index between
300 and 700 nanometers for Mt. St. Helenes ash, *Science, 211*, 836-838, 1981.

Penner, J.E., R. Dickinson, and C. O'Neill, Effects of aerosol from biomass burning on the global radiation budget, *Science, 256*, 1432-1434, 1992.

Pilinis, C., S.N. Pandis, and J.H Seifeld, Sensitivity of direct climate forcing by atmospheric aerosols to aerosol size and composition, *J. Geophys. Res.*, 100, 18,739-18,754, 1995.

Podgorny, I.A., A.M. Vogelmann, and V. Ramanathan, Effects of cloud shape and water vapor distribution on solar absorption in the near infrared, *Geophys. Res. Lett., 25*, 1899-1902, 1998.

Podgorny, I.A., W.C. Conant, V. Ramanathan, and S.K. Satheesh, Aerosol modulation of atmospheric and surface solar heating rates over the Tropical Indian Ocean, *Tellus*, 1999, in press.

Prodi, F., G. Santachiara, and F. Oliosi, Characterisation of aerosols in remote environments (Mediterranean, Red Sea, and Indian Ocean), *J. Geophys. Res., 88*, 10,957-10,968, 1983.

Prospero, J.M., Mineral and sea-salt aerosol concentrations in various oceanic regions, *J. Geophys. Res., 84*, 725-731, 1979.

Prospero, J.M., H. Maring, and D. Savoie, Aerosol chemical composition, light scattering and light absorption in the Maldive islands during the Indian Ocean winter monsoon: The impact of continental sources on aerosol radiative properties, Paper presented at INDOEX Workshop Meeting, INDOEX Int. Project Office, La Jolla, Calif., July 1998.

Pruppacher, H.R., and J.D. Klett, *Microphysics of Clouds and Precipitation*, pp. 364-371, D. Reidel, Norwell, Mass., 1978.

Pszenny, A., D. Fischer, A. Mendez, and M. Zetwo, Direct comparison of celluloid and quartz fiber filters for sampling submicrometer aerosols in the marine boundary layer, *Atmos. Environ., 27*, 281-284, 1993.

Quinn, P.K., S.F. Marshall, T.S. Bates, and D.S. Covert, and V.N. Kapustin, Comparison of measured and calculated aerosol properties relevant to the direct radiative forcing of troposphere sulfate aerosol on climate, *J. Geophys. Res., 100*, 8977-8992, 1995.

Quinn, P.K., V.N. Kapustin, T.S. Bates, and D.S. Covert, Chemical and optical properties of marine boundary layer aerosol particles of the mid-Pacific in relation to sources and meteorological transport, *J. Geophys. Res., 101*, 6931-6951, 1996.

Quinn, P.K., D.J. Coffman, V.N. Kapustin, T.S. Bates, and D.S. Covert, *J. Geophys. Res., 103*, 16,547-16,564, 1998.

Ramanathan, V., et al., Cloud radiative forcing and climate: Results

from the Earth Radiation Budget Experiment, *Science, 243*, 57-63, 1989.

Ramanathan, V., et al., Indian Ocean Experiment (INDOEX), Pap. $C^4$, Scripps Inst. of Oceanogr., La Jolla, Calif., 1995.

Ramanathan, V., et al., Indian Ocean Experiment (INDOEX), A multi-agency proposal for field experiment in the Indian Ocean, $C^4$ *publ. 162*, 83 pp., Scripps Inst. of Oceanogr., La Jolla, Calif., 1996.

Rau, J.A., Composition and size distribution of residential wood smoke particles, *Aerosol Sci. Technol., 10*, 181-192, 1987.

Remer, L.A., and Y.J. Kaufman, Dynamic aerosol model: Urban/industrial aerosol, *J. Geophys. Res., 103*, 13,859-13,871, 1998.

Satheesh, S.K., and K.K. Moorthy, Aerosol characteristics over coastal regions of the Arabian Sea, *Tellus, Ser. B, 49*, 417-428, 1997.

Satheesh, S.K., K. Krishna Moorthy, and B.V. Krishna Murthy, Spatial gradients in aerosol characteristics over the Arabian Sea and Indian Ocean, *J. Geophys. Res., 103*, 26,183-26,192, 1998.

Savoie, D.L., and J.M. Prospero, Particle size distribution of nitrate and sulfate in the marine atmosphere, *Geophys. Res. Lett., 9*, 1207-1210, 1982.

Savoie, D.L., J.M. Prospero, and E.S. Saltzman, Non-sea-salt sulfate and nitrate in trade wind aerosols at Barbados: Evidence for long range transport, *J. Geophys. Res., 94*, 5069-5080, 1989.

Shah, J.J., R.L. Johnson, E.K. Heyerdahl, and J.J. Huntzicker, Carbonaceous aerosol at urban and rural sites in the United States, *J. Air Pollut. Control Assoc., 36*, 254-257, 1986.

Shaw, G.E., J.A. Regan, and B.M. Herman, Investigations of atmospheric extinctions using direct solar radiation measurements made with a multiple wavelength radiometer, *J. Appl. Meteorol., 12*, 374-380, 1973.

Shi, L., Cloud radiative forcing on surface short wave fluxes: A case study based on Cloud Lidar and Radar Exploratory Test, *J. Geophys. Res., 99*, 25,909-25,921, 1994.

Shrestha, R.P., Light scattering by aerosol particles at an anthropogenically perturbed, mid latitude, continental site and its dependence on particle mass, composition, and air mass trajectory, M.S. thesis, 130 pp., Univ. of Ill. Urbana-Champaign, 1996.

Tegen, I., P. Hollrig, M. Chin, I. Fung, D. Jacob, and J. Penner, Contribution of different aerosol species to the global aerosol extinction optical thickness: Estimates from model results, *J. Geophys. Res., 102*, 23,895-23,914, 1997.

Turpin, B.J., J.J. Huntzicker, S.M. Larson, and, G. R. Cass, Los Angeles summer midday particulate carbon: Primary and secondary aerosol, *Environ. Sci. Technol., 25*, 1788-1793, 1991.

Twomey, S., Introduction to the mathematics of inversion in remote sensing and indirect measurements, in Developments in Geomathematics, *Elsevier Sci.*, New York, 1977.

Tyson, P.D., M. Garstang, R. Swap, P.Kallberg, and N. Edwards, An air transport climatology for subtropical southern Africa, *Int. J. Climatol., 16*, 256-291, 1996.

Waggoner, A.P., A.J. Vanderpol, R.J. Charlson, S. Larsen, L. Granet, and C. Tragardh, Sulfate-light scattering ratio as an index of the role of sulfur in tropospheric optics, *Nature, 261*, 120-122, 1976.

Weilicki, B.A., B.R. Barkstrom, E.F. Harrison, R.B. Lee III, G.L Smith, and J.E. Cooper, Clouds and the Earth's Radiant Energy System (CERES): An Earth observing system experiment, *Bull. of Am. Meeorol. Soc., 77*, 853-868, 1996.

White, W.H., Apportioning fine-particle scattering to chemical fractions, in Visibility: Existing and Historical Conditions – Causes and Effects, Vol. 24, edited by J.C. Trijonis, U.S. Natl. Acid Precip. Assess. Program, Washington, D.C., pp. 94-99, 1990.

B.N. Holben, NASA Goddard Space Flight Center, Code 923,Greenbelt, MD 20771, USA.

X.Li-Jones, J.M. Lobert, I.A. Podgorny, V. Ramanathan (corresponding author), S.K. Satheesh, Scripps Institution of Oceanography, University of California, San Diego, 9500 Gilman Drive, La Jolla, CA 92093-0221 (ram@fiji.ucsd.edu).

N.G. Loeb, NASA Langley Research Center, Mail Stop 420, 21 Langley Boulevard, Hampton, VA 23681.

J.M. Prospero, Rosenstiel School of Marine and Atmospheric Science, University of Miami, 4600 Rickenbacker Causeway, Miami, FL 33149, USA.

Received December 7, 1998; revised April 29, 1999;
Accepted June 18, 1999